



HAL
open science

Nanoarchitectonics of Glass Coatings for Near-Infrared Shielding: From Solid-State Cluster-Based Niobium Chlorides to the Shaping of Nanocomposite Films

Clément Lebastard, Maxence Wilmet, Stéphane Cordier, C. Comby-Zerbino, Luke Macaleese, Philippe Dugourd, Tetsuo Uchikoshi, Vincent Dorcet, Maria Amela-Cortes, Adèle Renaud, et al.

► To cite this version:

Clément Lebastard, Maxence Wilmet, Stéphane Cordier, C. Comby-Zerbino, Luke Macaleese, et al.. Nanoarchitectonics of Glass Coatings for Near-Infrared Shielding: From Solid-State Cluster-Based Niobium Chlorides to the Shaping of Nanocomposite Films. *ACS Applied Materials & Interfaces*, 2022, 14 (18), pp.21116-21130. 10.1021/acsami.2c00308 . hal-03681057

HAL Id: hal-03681057

<https://hal.science/hal-03681057>

Submitted on 5 Oct 2022

HAL is a multi-disciplinary open access archive for the deposit and dissemination of scientific research documents, whether they are published or not. The documents may come from teaching and research institutions in France or abroad, or from public or private research centers.

L'archive ouverte pluridisciplinaire **HAL**, est destinée au dépôt et à la diffusion de documents scientifiques de niveau recherche, publiés ou non, émanant des établissements d'enseignement et de recherche français ou étrangers, des laboratoires publics ou privés.

Nanoarchitectonics of Glass Coatings for Near-Infrared Shielding: From Solid-State Cluster-Based Niobium Chlorides to the Shaping of Nanocomposite Films

Clément Lebastard,^{a,b,‡} Maxence Wilmet,^{b,a,c,‡} Stéphane Cordier,^{a,} Clothilde Comby-Zerbino,^d Luke MacAleese,^d Philippe Dugourd,^d Tetsuo Uchikoshi,^{b,e} Vincent Dorcet,^a Maria Amela-Cortes,^a Adèle Renaud,^a Karine Costuas,^{a,*} Fabien Grasset^{b,a}*

^a Univ Rennes, CNRS, ISCR (Institut des Sciences Chimiques de Rennes) – UMR 6226, F-35000 Rennes, France.

^b CNRS – Saint-Gobain – NIMS, IRL 3629, Laboratory for Innovative Key Materials and Structures (LINK), National Institute for Materials Science, 1-1 Namiki, 305-0044 Tsukuba, Japan

^c Saint-Gobain Research Paris, F-93300 Aubervilliers, France.

^d Univ Lyon, Université Claude Bernard Lyon 1, ENS de Lyon, Institut des Sciences Analytiques, UMR 5280, 5 rue de la Doua, F-69100 Villeurbanne, France.

° Research Center for Functional Materials, National Institute for Materials Science (NIMS), 1-1
Namiki, Tsukuba, Japan.

* Emails: karine.costuas@univ-rennes1.fr; stephane.cordier@univ-rennes1.fr

KEYWORDS: Inorganic Chemistry, Nanocomposite films, Nanoarchitectonics, Metal Atom Clusters, Niobium, Cluster-Based Hybrid Nanomaterials, Near-Infrared Shielding

ABSTRACT: The high potential of $[\{\text{Nb}_6\text{Cl}^i_{12}\}\text{L}^a_6]$ cluster-based building blocks as near-infrared radiation blockers for energy saving applications is exposed in the present paper (i = inner edge-bridging ligand, a = apical ligand of the Nb_6 ; $\text{L} = \text{H}_2\text{O}$ and/or Cl). To do so, a combined experimental and theoretical investigation of edge-bridged $[\{\text{Nb}_6\text{Cl}^i_{12}\}\text{Cl}^a_{6-x}(\text{H}_2\text{O})_x]^{m+/0/n-}$ cluster unit series ($x = 0, 4, 6$; $m = 2, 3, 4$; $n = 2, 3, 4$) has been carried out. By using the $\text{K}_4[\{\text{Nb}_6\text{Cl}^i_{12}\}\text{Cl}^a_6]$ starting solid-state precursor, we explored the behavior of the $[\{\text{Nb}_6\text{Cl}^i_{12}\}\text{Cl}^a_6]^{4-}$ cluster unit during the different steps of their integration as building block into a polyvinylpyrrolidone (PVP) matrix to form a glass coating composite denoted $\{\text{Nb}_6\text{Cl}^i_{12}\}^{m+}@PVP$ ($m = 2$ or 3). The optical, vibrational and redox properties $[\{\text{Nb}_6\text{Cl}^i_{12}\}\text{Cl}^a_{6-x}(\text{H}_2\text{O})_x]^{m+/0/n-}$ building blocks have been interpreted with the support of electronic structure calculations and simulation of properties. The chemical modifications and oxidation properties have been identified and studied thanks to various techniques in solution. Combining Raman and ultraviolet-visible spectroscopies, electrochemistry and quantum chemical simulations, we bring new knowledge to the understanding of the evolution of the properties of the $[\{\text{Nb}_6\text{Cl}^i_{12}\}\text{Cl}^a_{6-x}(\text{H}_2\text{O})_x]^{m+/0/n-}$ cluster units as function of the number of valence electron per cluster (VEC) and the nature of terminal ligands ($x = 0, n = 4$; $x = 4$, charge = 0; $x = 6, m = 4$). The fine understanding of the physical properties and vibrational fingerprints depending on the VEC and chemical modifications in solution are mandatory to master the

processing of cluster-based building blocks for the controlled design and shaping of glass coating nanocomposites. Based on this acquired knowledge, $[\{\text{Nb}_6\text{Cl}_{12}^{\text{i}}\}\text{Cl}_{6-x}(\text{H}_2\text{O})_x]^{m+/0/n-}$ building blocks were embedded in a PVP matrix. The resulting $\{\text{Nb}_6\text{Cl}_{12}^{\text{i}}\}^{2+}@PVP$ nanocomposite film shows excellent ultraviolet (UV, 280-380 nm) and near-infrared (NIR, 780-1080 nm) blocking ability (> 90%) and a highly visible light transmittance thanks to the controlled integration of the $\{\text{Nb}_6\text{Cl}_{12}^{\text{i}}\}^{2+}$ cluster core. The figures of merit (FOM) value of $T_{\text{vis}}/T_{\text{sol}}$ (T_{vis} = visible transmittance and T_{sol} = solar transmittance) as well as the haze, clarity and the NIR shielding values (S_{NIR}) were measured. After optimization of the integration process, a $\{\text{Nb}_6\text{Cl}_{12}^{\text{i}}\}^{2+}@PVP$ nanocomposite on glass substrate has been obtained with a high FOM equal to 1.29. This high value places the transparent green olive $\{\text{Nb}_6\text{Cl}_{12}^{\text{i}}\}^{2+}@PVP$ nanocomposites at the top system in the benchmark in the field of glass coating composites for energy saving applications.

1. INTRODUCTION

On the one hand, the solar energy distribution on the earth's surface, which is slightly different than that measured at the top of the atmosphere, is approximately composed by 5% UV radiation (280-400 nm), 43% visible radiation (400-700 nm) and around 52% NIR radiation (700-3000 nm).¹ On the other hand, thermal transfers in buildings (*i.e.* heating, air conditioning and ventilation) represent at least 50% of the global building energy use.² That is why reducing the energy consumption and particularly the excess of solar heat gain is a key point in the global warming prevention solution. Nowadays, several nanomaterial-based cool coatings have demonstrated their potential in solar control.³ In order to increase the solar-reflecting and/or the solar-absorptive function, which mainly relies on NIR, new transparent inorganic materials based on metal, metal oxide or metalloid have been developed in the last decades.³ Indium and antimony tin oxides (ITO

and ATO) are largely studied for their NIR reflective ability,^{4,5} while tungsten bronze oxides are developed and exploited for their NIR absorption property.⁶ Metal oxides have the advantage to confer both reflection and absorption properties in bulk composite materials and when shaped in glass coating films. Among the emerging materials, the octahedral cluster compounds do present interesting radiation blocking ability but their potential for solar control has been scarcely studied.^{7,8} They are prepared by solid-state reaction at high temperatures and are commonly built from metal atoms of the fifth and sixth columns of the periodic table (M = Nb, Ta, Mo and W) stabilized by halogen ligands (X = Cl, Br, I). Among those systems, the edge-bridged cluster units of formula [$\{M_6X^{i}_{12}\}X^a_6$] are known to be strong redox agents and UV-absorbents.⁹ They have been used as precursors for the syntheses of a wide range of hybrid compounds exhibiting unusual structural arrangements¹⁰⁻¹⁸ as well as for the syntheses of some composites presenting catalytic¹⁹ or energy saving abilities.^{7,8,20} Their true nanosized, strong molecular character and very good solubility in water or in several organic solvents makes them very easy to be processed as nanocomposites. This gives them significant advantages over the most common solar control IR absorbers since solutions are often involved in low-cost synthetic processes to fabricate the final materials.

In the present study, the potential of edge-bridged niobium cluster chlorides as near infrared blockers for energy saving applications is investigated. Using $K_4[\{Nb_6Cl^{i}_{12}\}Cl^a_6]$ as cluster precursor, the evolutions of the [$\{Nb_6Cl^{i}_{12}\}Cl^a_6$]⁴⁻ units in terms of apical ligand exchanges and oxidation states were tracked from the solid-state to solution and all along the pathways of integration in PVP-based composites. Combining Raman and UV spectroscopies, electrochemistry and quantum chemical simulations, the vibrational and absorption properties of cluster units in the solid-state and in solution were investigated as a function of the oxidation state of the $\{Nb_6Cl^{i}_{12}\}^{m+}$

cluster core, the valence electron count (VEC) and its apical ligand environment. These fundamental investigations enabled the rational design of a $\{\text{Nb}_6\text{Cl}_{12}\}^{2+}@PVP$ nanocomposite films with optimized NIR absorption. Glass coating composites have been prepared from this material and characterized.

2. SYNTHESSES AND CHARACTERIZATIONS

Several methods have been published in the literature for the preparation of $\text{K}_4[\{\text{Nb}_6\text{Cl}_{12}\}\text{Cl}_6^{\text{a}}]$ with different reaction times and reaction temperatures leading to different yields of reaction as presented in SI. The advantages and drawbacks of the reported preparation methods are presented in SI. In this work, the synthesis of $\text{K}_4[\{\text{Nb}_6\text{Cl}_{12}\}\text{Cl}_6^{\text{a}}]$ by reduction of NbCl_5 by Nb in the presence of KCl was improved in order to obtain the lowest cost one-pot reaction, to reach the highest yields associated with the lowest possible temperature and time of reaction. The crude product of this reaction is designated **1** from now. The aim of this work being the controlled integration of cluster units into matrices, the full understanding of the behavior of the cluster units in solution is highly crucial to optimize the elaboration procedures and the resulting properties. The synthesis of the solid-state compounds, *i.e.* $[\{\text{Nb}_6\text{Cl}_{12}\}\text{Cl}_2(\text{H}_2\text{O})_4^{\text{a}}]\cdot 4\text{H}_2\text{O}$ (**2**) built up from a cluster-based aquo-complex and $(\text{TBA})_3[\{\text{Nb}_6\text{Cl}_{12}\}\text{Cl}_6^{\text{a}}]$ (**3**) built up from a halide complex, resulting from the dissolution in water and in acetone respectively of the crude product of reaction **1** containing $\text{K}_4[\{\text{Nb}_6\text{Cl}_{12}\}\text{Cl}_6^{\text{a}}]$ are presented below and gathered in Scheme 1. Following these dissolution processes, the different routes of integration of $\{\text{Nb}_6\text{Cl}_{12}\}^{2+, 3+}$ -containing clusters in PVP matrix are also summarized in Scheme 1. Full details are given in the supporting information (SI).

excess, proposed by Parsons *et al.*²² to 2.3. The X-ray powder diffraction analysis of crude **1**, proved that $K_4[\{Nb_6Cl^{i}_{12}\}Cl^a_6]$ is the major product and also evidenced the presence of unreacted KCl and Nb as secondary phases. The refinement of the X-ray powder pattern of the $K_4[\{Nb_6Cl^{i}_{12}\}Cl^a_6]$ phase (Figure S1) fully agree with the crystallographic data (space group $C2/m$, (No. 12), $a = 9.97(3) \text{ \AA}$, $b = 16.51(5) \text{ \AA}$, $c = 9.47(3) \text{ \AA}$, $\beta = 115.0(5)$) reported by A. Simon *et al.*²³ that were obtained by single crystal X-ray diffraction (XRD) means. The refined unit cell parameters of $K_4[\{Nb_6Cl^{i}_{12}\}Cl^a_6]$ in **1** are the following: $a = 9.96(6) \text{ \AA}$, $b = 16.54(7) \text{ \AA}$, $c = 9.45(0) \text{ \AA}$, $\beta = 114.81(8)^\circ$. The broadness of the diffraction peaks did not enable the refinement of the atomic coordinates. The composition of **1** was determined following the analysis presented in SI. **1** includes 62.5 % $K_4[\{Nb_6Cl^{i}_{12}\}Cl^a_6]$, 22.0 % KCl, and 15.5 % Nb. For a typical batch of **1** obtained with 3.2 g of loaded reactant mixture, the final weight of $K_4[\{Nb_6Cl^{i}_{12}\}Cl^a_6]$ is 2 g (yield ≈ 80 %). The synthesis is fully reproducible. Note that **1** is rather sensitive to moisture and to air oxidation.

2.2. Behavior of $K_4[\{Nb_6Cl^{i}_{12}\}Cl^a_6]$ in water. The dissolution of **1** in water (Scheme 1) leads to a green olive solution called **1_{water}** thereafter. The filtration of **1_{water}** enables to eliminate unreacted Nb metal. The investigations of filtrated **1_{water}** by mass spectrometry (Figure 1) were carried out in both positive and negative modes. Interestingly, although **1** contains negatively-charged cluster units $[\{Nb_6Cl^{i}_{12}\}Cl^a_6]^{4-}$, only positive ions were detected. The major detected ion is the $[\{Nb_6Cl^{i}_{12}\}(H_2O)^a_6]^{2+}$ cluster units which corresponds to a $\{Nb_6Cl^{i}_{12}\}^{2+}$ core (VEC = 16). The second detected species are $[\{Nb_6Cl^{i}_{12}\}(H_2O)^a_5]^{2+}$ cations which originate from the $[\{Nb_6Cl^{i}_{12}\}(H_2O)^a_6]^{2+}$ ions after the loss of one water molecule. These results indicate that $[\{Nb_6Cl^{i}_{12}\}Cl^a_6]^{4-}$ are not stable in water and that the apical Cl^- ligands are readily replaced by water molecules to form the most water stable $[\{Nb_6Cl^{i}_{12}\}(H_2O)^a_6]^{2+}$ cationic units. Recall that a

similar behavior was observed when dissolving in water the parent tantalum bromide compound $K_4[\{Ta_6Br^{i}_{12}\}Br^a_6]$.²⁴ Replacing Cl^- ligands of $[\{Nb_6Cl^i_{12}\}Cl^a_6]^{4-}$ by water molecules does not lead to any change of oxidation of the cluster core whose VEC remains at the value of 16.

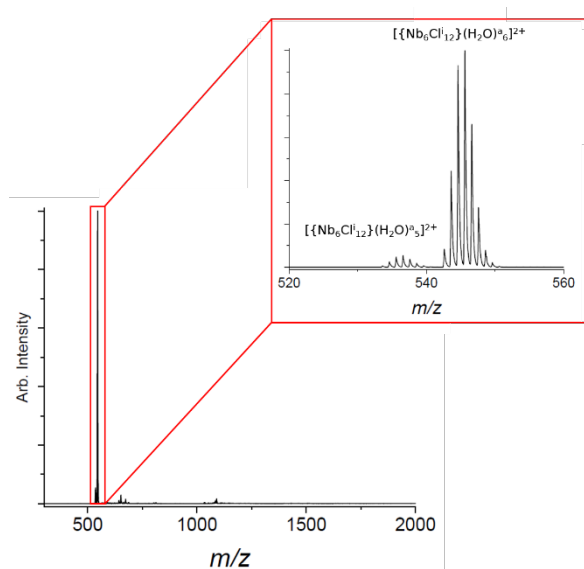


Figure 1. Mass spectrum of $\mathbf{1}_{\text{water}}$ in positive mode.

2.3. Synthesis of $[\{Nb_6Cl^i_{12}\}Cl^a_2(H_2O)^a_4] \cdot 4H_2O$ (**2**) and acidic properties in water solution.

$[\{Nb_6Cl^i_{12}\}Cl^a_2(H_2O)^a_4] \cdot 4H_2O$ was prepared from **1** according to a derived protocol described by Koknat *et al.*²⁵ (detailed in SI) but in which a different precursor, $Na_4[\{Nb_6Cl^i_{12}\}Cl^a_6]$, was used. The synthetic protocol is described in Scheme 1. After the dissolution of **1** in water and further filtration, hydrochloric acid was added in $\mathbf{1}_{\text{water}}$ to favor the precipitation of $[\{Nb_6Cl^i_{12}\}Cl^a_2(H_2O)^a_4] \cdot 4H_2O$. Note that in this protocol, it is necessary to heat the solution and to add stannic chloride in order to avoid the oxidation of the $\{Nb_6Cl^i_{12}\}^{2+}$ core. Indeed, at room temperature, $\mathbf{1}_{\text{water}}$ is stable but the oxidant ability of the medium increases by combining heating and addition of hydrochloric acid. As demonstrated earlier for the parent $[\{Ta_6Br^i_{12}\}Br^a_2(H_2O)^a_4] \cdot 4H_2O$, the crystallization process involves the formation of zero charged cluster units $[\{Nb_6Cl^i_{12}\}Cl^a_2(H_2O)^a_4]^0$ containing two apical halogen ligands and four apical water

molecules.²⁴ The resulting aquo solid-state compounds are $[\{\text{Nb}_6\text{Cl}^{\text{i}}_{12}\}\text{Cl}^{\text{a}}_2(\text{H}_2\text{O})^{\text{a}}_4]\cdot 4\text{H}_2\text{O}$ as already reported.²⁵ No XRD structural resolution has been reported to date for this system. The X-ray powder diffraction pattern was recorded (Figure S2). It is highly comparable to that published by Chihara and coworkers.¹⁹ Unfortunately, the quality of the diffraction pattern did not allow any structural resolution and further refinements.

As demonstrated below, the dissolution of $[\{\text{Nb}_6\text{Cl}^{\text{i}}_{12}\}\text{Cl}^{\text{a}}_2(\text{H}_2\text{O})^{\text{a}}_4]\cdot 4\text{H}_2\text{O}$ in water leads to a solution of the stable species $[\{\text{Nb}_6\text{Cl}^{\text{i}}_{12}\}(\text{H}_2\text{O})^{\text{a}}_6]^{2+}$ containing six apical water molecules. The poly-acidic property of $[\{\text{Nb}_6\text{Cl}^{\text{i}}_{12}\}(\text{H}_2\text{O})^{\text{a}}_6]^{2+}$ was evaluated by performing the titration of a $2.2 \cdot 10^{-3} \text{ mol}\cdot\text{L}^{-1}$ fresh aqueous solution of **2** by a KOH solution ($1.6 \cdot 10^{-2} \text{ mol}\cdot\text{L}^{-1}$). The initial pH was ≈ 2.75 . The first pKa was estimated to be 3.2. The second pKa could not be measured because of the precipitation of $[\{\text{Nb}_6\text{Cl}^{\text{i}}_{12}\}(\text{H}_2\text{O})^{\text{a}}_4(\text{OH})^{\text{a}}_2]^0$ species during the measurement.

2.4. Behavior of $\text{K}_4[\{\text{Nb}_6\text{Cl}^{\text{i}}_{12}\}\text{Cl}^{\text{a}}_6]$ in acetone. Dissolving **1** in acetone results in a solution which color depends on whether the dissolution has been prepared under oxygen-free atmosphere or not. Under an inert atmosphere using Schlenk tube techniques, the solution exhibits a green olive color. The solution turns instantaneously to brown when exposed to air. The dissolution under atmospheric condition leads to the same brown solution, **1**_{acetone}. This solution was filtrated to remove the unreacted Nb and KCl salts present in **1**. It was analyzed by mass spectrometry in negative and positive modes (Figure 2). No ion was detected in positive mode. Two species were detected in negative mode: $[\{\text{Nb}_6\text{Cl}^{\text{i}}_{12}\}\text{Cl}^{\text{a}}_6]^{2-}$ and $[\{\text{Nb}_6\text{Cl}^{\text{i}}_{12}\}\text{Cl}^{\text{a}}_5]^{2-}$. These species correspond to a $\{\text{Nb}_6\text{Cl}^{\text{i}}_{12}\}$ -oxidized species associated VEC of 14 and 15 respectively. Contrarily to water solution, the dissolution in acetone does not lead to the substitution of the Cl apical ligands by water molecules but to the oxidation of the cluster core.

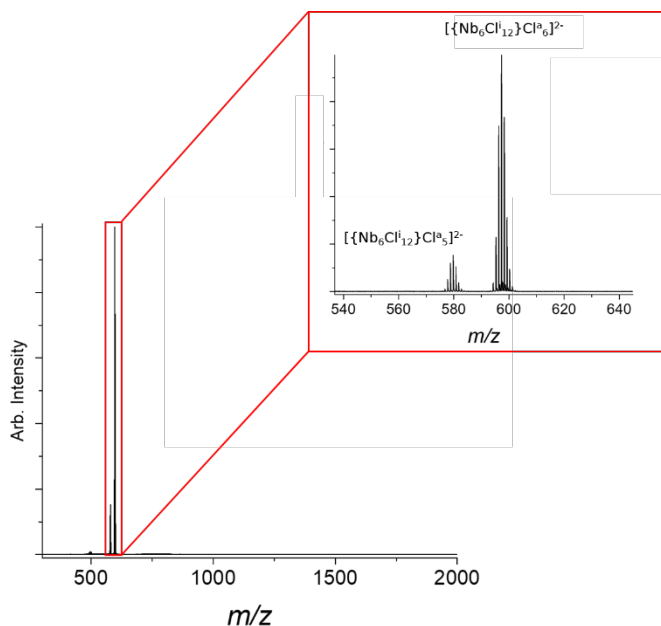


Figure 2. Mass spectrum of **1**_{acetone} in negative mode.

2.5. Optimized synthesis and structural characterizations of (TBA)₃[{Nb₆Clⁱ₁₂}Cl^a₆] (3**).** It is worth noting that the methods reported in the literature for the synthesis of A_x[{Nb₆Clⁱ₁₂}Cl^a₆] compounds (A = (C₂H₅)₄N, (C₄H₉)₄N, ((C₂H₅)₂O)₂H) are intricate multistep protocols.^{18, 26–28} The starting precursors in all these reported syntheses are the aquo complexes [{Nb₆Clⁱ₁₂}Cl^a₂(H₂O)^a₄]·nH₂O (n = 3, 4) obtained from Na₄[{Nb₆Clⁱ₁₂}Cl^a₆] or K₄[{Nb₆Clⁱ₁₂}Cl^a₆]. The substitution of water molecules by Cl⁻ ions to afford back fully chlorinated [{Nb₆Clⁱ₁₂}Cl^a₆]ⁿ⁻ cluster units is not straightforward. It is carried out under reflux in ethanol solution for reduced species (n = 4) and under reflux in ethanol with a saturated HCl solution to obtain oxidized species (n = 3). An extra treatment with thionylchloride in the presence of an excess of diethyl ether and 18-crown-6 has been more recently proposed to synthesize [(Et₂O)₂H]₂[{Nb₆Clⁱ₁₂}Cl^a₆].¹⁸

We report here a much simpler synthesis which uses the one-pot reaction starting from product **1** to obtain (TBA)₃[{Nb₆Clⁱ₁₂}Cl^a₆], **3** (TBA⁺ = [N(C₄H₉)₄]⁺). It is prepared by a simple cationic metathesis by addition of (TBA)Cl to filtered **1**_{acetone} (SI). Single crystals of **3** are obtained by ether

diffusion in this solution. The structural resolution is fully detailed in SI. **3** crystallizes in the $P2_1/m$ space group (No. 11) with the refined unit cell parameters: $a = 13.8221(1) \text{ \AA}$, $b = 22.8804(2) \text{ \AA}$, $c = 24.5205(1) \text{ \AA}$, $\beta = 101.648(2)^\circ$. A CIF file containing the crystallographic data of **3** was deposited at CCDC under the quotation CCDC 2125347. These data can be obtained free of charge from the Cambridge Crystallographic Data Centre via www.ccdc.cam.ac.uk/data_request/cif. Bond lengths in **3** are comparable to those published for $(\text{TMA})_3[\{\text{Nb}_6\text{Cl}_{12}\}\text{Cl}_6]$ ($\text{TMA}^+ = [\text{N}(\text{CH}_3)_4]^+$)²⁹ which is also built-up from $[\{\text{Nb}_6\text{Cl}_{12}\}\text{Cl}_6]^{3-}$ anionic units of VEC = 15. The cyclic voltammograms of a solution of **3** in dichloromethane (**3**_{DCM}) were recorded as detailed in SI (Experimental procedures and Figure S3). The starting potential is in agreement with a 15-VEC. Two reversible one-electron transfers were observed at -0.20 and 0.33 V vs Ag/AgCl (for comparison: + 0.208 and + 0.738 V vs ferrocenium/ferrocene), in agreement with the values reported by Prokopuk *et al.*³⁰ and Pénicaud *et al.*³¹

2.6. Raman spectroscopy analysis. The Raman spectra of **1** (powder), **1**_{water} (solution), **2** (powder) and **3** (single-crystals) are gathered in Figure 3. They were recorded following the procedure given in the experimental section. Spectra were recorded for two different synthetic batches of **1** and **3** in order to confirm the reproducibility of the syntheses. The spectra are very similar from one batch to another with only slight differences in the peak intensities owing to the resolution quality. This confirms the reproducibility of the syntheses. Regardless the shifts of the peak positions and their intensities, the Raman spectra of **1** and **3** are highly similar. The vibrational modes found in the low-energy region between 100 and 400 cm^{-1} are attesting the presence of cluster units. In that region, the Raman spectra of **1** and **3** are both presenting intense peaks at 143-144 cm^{-1} and 196-199 cm^{-1} . One can note that the Raman signature of **3** can be differentiated from that of **1** by two intense characteristic peaks at 271 and 360 cm^{-1} observed for **3**. The Raman

spectrum of **1** also contains these peaks but their intensities are very weak. The most intense peak of **1** in this region is located around 255-256 cm^{-1} .

The Raman spectra of water solutions of **1**, *i.e.* **1_{water}**, were recorded at different aging times. They hardly change with time revealing the stability of the system in aqueous solutions (see Figure 3). These spectra are less well resolved than the spectra of **1** and **3** in the solid-state but the bands located under 400 cm^{-1} undoubtedly reveal the integrity of cluster units in solution. The peak at 144 cm^{-1} which is also found for **1** and **3** is also present. A second peak at 229 cm^{-1} is distinctly observed from the base line. It is not present in **1** and **3** spectra. This peak is thus characteristic of the cluster unit species in **1_{water}** for which mass spectrometry revealed that all Cl^- apical ligands are substituted by water molecules. The comparison with the solid-state Raman spectrum of **2** which contains $[\{\text{Nb}_6\text{Cl}_{12}\}\text{Cl}_2(\text{H}_2\text{O})_4]^{2+}$ units is thus interesting. First, a vibrational absorption peak at 168 cm^{-1} reminds the 161 cm^{-1} peak of **1** and might be related to $\text{VEC} = 16$ cluster units. It is not observed for **3**. Secondly, an intense vibrational absorption peak is found at 231 cm^{-1} , similarly as for **1_{water}**. An extra peak at 216 cm^{-1} clearly differentiates the experimental spectra of **1_{water}** and **2**. Further interpretations will be given below on the basis of absorption spectra and computational results.

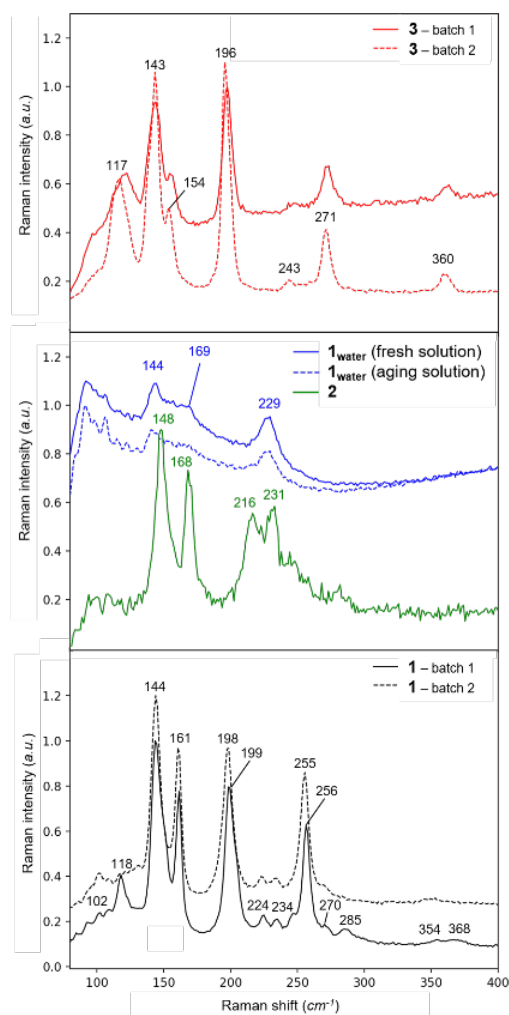


Figure 3. Normalized Raman spectra of **1** for two different batches with different aging times (bottom, black), of **1_{water}** and **2** (middle blue and green respectively) and of **3** for two different synthesis batches (top, red). For more convenience, baselines have been modified: **1** – batch 2: +0.2 a. u., **1_{water}** – fresh: +0.1 a. u., **2**: -0.1 a. u., **3** – batch 2: +0.1 a. u.

2.6. UV-vis absorption spectra of 1 and 3 in water, acetone and DCM. UV-vis absorption spectra of **1_{water}** and **1_{acetone}** are reported in Figure 4 (left). The main absorption peak in the UV region is located at 398 nm and 445 nm for **1_{water}** and **1_{acetone}** respectively. In the NIR region, a large peak at 899 nm is observed for **1_{water}** whereas **1_{acetone}** presents a peak at 1010 nm and a large

peak shoulder around 1289 nm. The spectra of **2_{water}** is superimposable with that of **1_{water}**. This finding means that whatever the starting compound, $K_4[\{Nb_6Cl^{i}_{12}\}Cl^a_6]$ or $[\{Nb_6Cl^{i}_{12}\}Cl^a_2(H_2O)^a_4] \cdot 4H_2O$, after solubilization in water, the solutions **2_{water}** and **1_{water}** contain the same species, *i. e.* $[\{Nb_6Cl^{i}_{12}\}(H_2O)^a_6]^{2+}$.

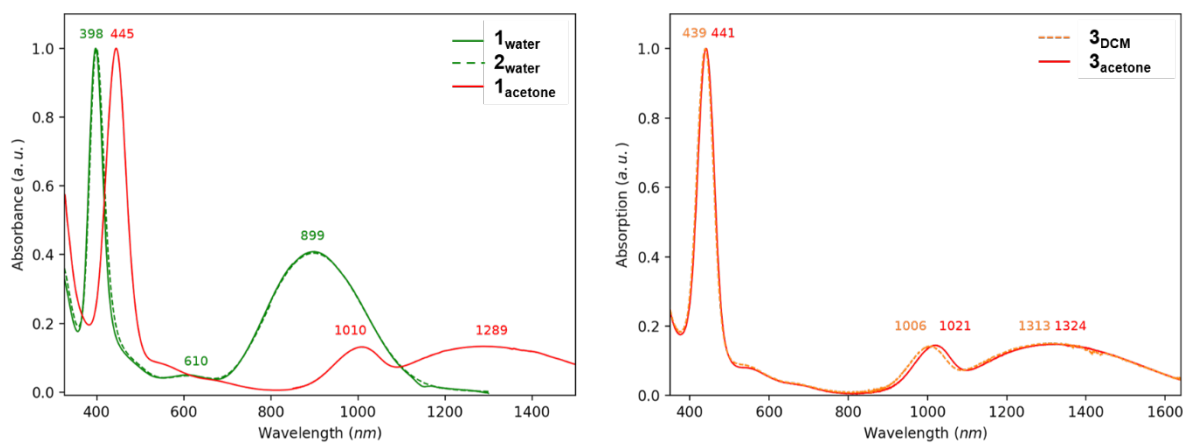


Figure 4. Left) Normalized UV-visible absorption spectra of **1_{water}**, **2_{water}** and **1_{acetone}**. Right) Normalized UV-visible absorption spectra of **3_{DCM}** and **3_{acetone}**.

Normalized UV-visible absorption spectra of **3_{acetone}** and **3_{DCM}** are reported in Figure 4 (right). Both spectra are almost superimposable. The band maxima of **3_{acetone}** and **3_{DCM}** are located at 439, 1006 and 1313 nm and 441, 1021 and 1324 nm respectively. The observed mean shift corresponds to an energy wavelength difference of 0.013 eV. This very low value is attributed to slight differences in solvation effects between acetone and DCM more than to ligand exchange or reduction/oxidation effect. Spectra of **1_{acetone}**, **3_{DCM}** and **3_{acetone}** are hardly differentiable considering the experimental uncertainty and resemble to the spectrum of $[\{Nb_6Cl^{i}_{12}\}Cl^a_6]^{3-}$ in acetone reported by Fleming *et al.*³². It can then be assumed that **1_{acetone}** and **3_{acetone}** contain the same species, *i. e.* $[\{Nb_6Cl^{i}_{12}\}Cl^a_6]^{3-}$.

3. COMPUTATIONAL RESULTS

Geometry optimizations of $[\{\text{Nb}_6\text{Cl}^{\text{i}}_{12}\}\text{Cl}^{\text{a}}_6]^{\text{n-}}$ units ($n = 2, 3, 4$) were carried out at the DFT level of theory (see computational details in SI). All three arrangements are presenting an O_h symmetry at 0 K in a vacuum. The main calculated distances are reported in Table 1 as well as selected experimental solid-state data issued from the crystal structures obtained by XRD investigations in previous studies^{17, 23, 27, 29, 33} and from the structure of **3** which has been solved in this work. The Cartesian coordinates of the optimized geometries are reported in Table S8. The Nb-Nb and Nb-Cl calculated distances agree with the experimental data with a maximum deviation of 3 %. A similar level of accuracy was already obtained for the Nb series by Kuc *et al.*³⁴ (Table 1). In the title work, the optimized interatomic distances better agree with the experimental structural data due to a slight improvement of the computational method (QZ4P basis set and revPBE functional instead of TZV basis set and PBE functional).

Noticeable bond length evolution appears in the $[\{\text{Nb}_6\text{Cl}^{\text{i}}_{12}\}\text{Cl}^{\text{a}}_6]^{\text{n-}}$ series upon oxidation state change. Starting from the VEC = 16 ($n = 4$), the Nb-Nb distance is increased by 0.048 Å and 0.046 Å for each successive oxidation, VEC = 15 ($n = 3$) and VEC = 14 ($n = 2$) respectively, whereas the Nb-Clⁱ bond lengths decreased by 0.017 Å and 0.015 Å. The Nb-Cl^a drastically decreases by 0.106 Å and 0.073 Å when n goes from 4 to 3 and 3 to 2 respectively.

The molecular orbital (MO) energy diagram of $[\{\text{Nb}_6\text{Cl}^{\text{i}}_{12}\}\text{Cl}^{\text{a}}_6]^{\text{n-}}$ cluster unit can be schematically depicted as a set of eight HOMOs presenting metal-metal bonding character and metal-ligand antibonding character separated by a substantial energy gap from a set of 16 unoccupied MOs, the first LUMOs, that are mainly metal-metal anti-bonding in character.³⁴ The oxidation of the cluster compound of VEC = 16 ($n = 4$) corresponds formally to the electron depopulation of the HOMO followed by an electronic and atomic relaxation. This loss of Nb-Nb

bonding and Nb-Cl antibonding characters induced by the depopulation the HOMO leads to the lengthening and shortening of these bond distances respectively. This is indeed what is calculated and observed experimentally (Table 1). It can be noticed that Nb-Nb and Nb-Cl bond lengths within the cluster units in **3** agree with those of (TMA)₃[{Nb₆Clⁱ₁₂}Cl^a₆], a 15-VEC compound (n = 3).²⁷

Table 1. Main bond length (Å) of the optimized geometries [$\{\text{Nb}_6\text{Cl}^i_{12}\}\text{Cl}^a_6\}^{n-}$ (n = 2-4) (O_h symmetry), [$\{\text{Nb}_6\text{Cl}^i_{12}\}(\text{H}_2\text{O})^a_6\}^{2+}$ and [$\{\text{Nb}_6\text{Cl}^i_{12}\}(\text{OH})^a_6\}^{4-}$, and of the available experimental XRD structures for sake of comparison. * = this work.

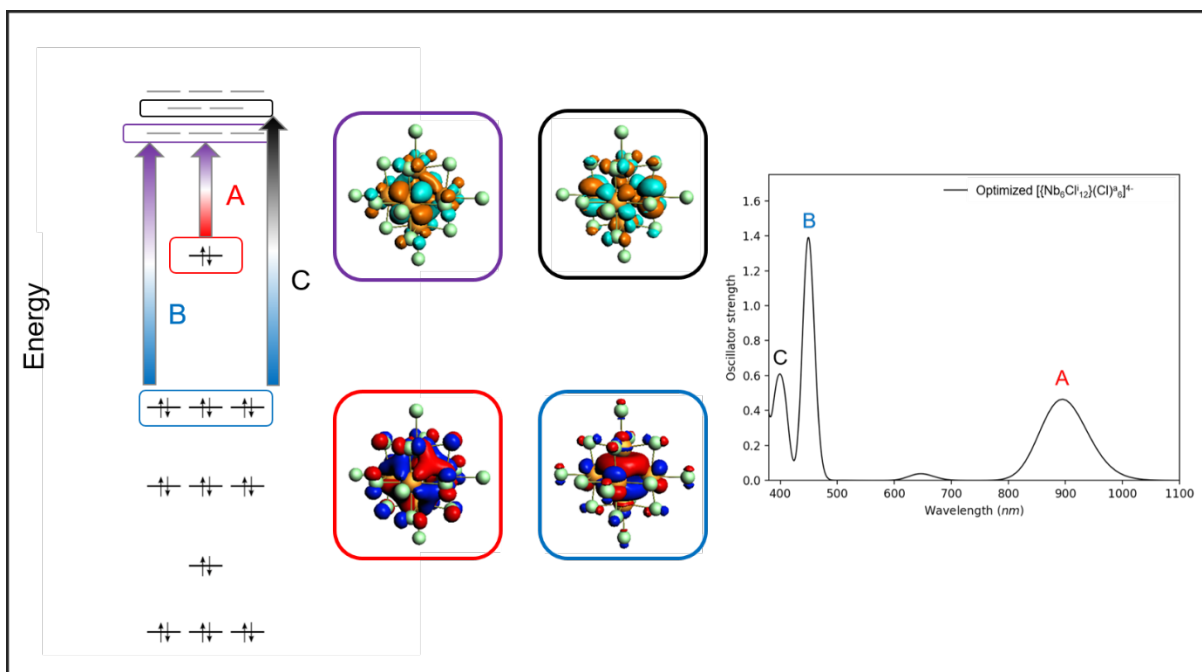
	Ref.	VEC	Nb-Nb	Nb-Cl ⁱ	Nb-Cl ^a	Nb-O ^a (H ₂)	Nb-O ^a (H)
<i>DFT optimized clusters</i>							
[{Nb ₆ Cl ⁱ ₁₂ }Cl ^a ₆] ⁴⁻	*	16	2.986	2.496	2.707		
[{Nb ₆ Cl ⁱ ₁₂ }Cl ^a ₆] ⁴⁻	[34]	16	2.995	2.512	2.697		
[{Nb ₆ Cl ⁱ ₁₂ }Cl ^a ₆] ³⁻	*	15	3.034	2.479	2.601		
[{Nb ₆ Cl ⁱ ₁₂ }Cl ^a ₆] ³⁻	[34]	15	3.041	2.491	2.537		
[{Nb ₆ Cl ⁱ ₁₂ }Cl ^a ₆] ²⁻	*	14	3.080	2.464	2.528		
[{Nb ₆ Cl ⁱ ₁₂ }Cl ^a ₆] ²⁻	[34]	14	3.084	2.474	2.537		
[{Nb ₆ Cl ⁱ ₁₂ }(\text{H}_2\text{O}) ^a ₆] ²⁺	*	16	2.910	2.485		2.375	
[{Nb ₆ Cl ⁱ ₁₂ }(\text{OH}) ^a ₆] ⁴⁻	*	16	3.018	2.543			2.152
<i>Experimental structures</i>							
K ₄ [{Nb ₆ Cl ⁱ ₁₂ }Cl ^a ₆]	[23]	16	2.92	2.48	2.61		
(TMA) ₃ [{Nb ₆ Cl ⁱ ₁₂ }Cl ^a ₆]	[29]	15	2.97	2.43	2.52		
(TBA) ₃ [{Nb ₆ Cl ⁱ ₁₂ }Cl ^a ₆] (3)	*	15	2.9955(5)	2.4339(1)	2.5311(6)		
(TMA) ₂ [{Nb ₆ Cl ⁱ ₁₂ }Cl ^a ₆]	[27]	14	3.018(2)	2.425(2) - 2.412(2)	2.46		
(TBA) ₂ [{Nb ₆ Cl ⁱ ₁₂ }Cl ^a ₆]	[17]	14	3.0357	2.4268	2.4913		
[Nb ₆ Cl ⁱ ₁₂ (\text{OH}) ^a ₂ (\text{H}_2\text{O}) ^a ₄].4\text{H}_2\text{O}	[33]	16	2.919 (×8) 2.901 (×4 basal)	2.433(2) - 2.478(2)		2.250(5)- 2.289(5)	2.147(5)

The geometrical arrangements of the aquo-cluster [$\{\text{Nb}_6\text{Cl}^i_{12}\}(\text{H}_2\text{O})^a_6\}^{2+}$ and the hydroxo-cluster [$\{\text{Nb}_6\text{Cl}^i_{12}\}(\text{OH})^a_6\}^{4-}$ were optimized by DFT following the same computational procedure as for the [$\{\text{Nb}_6\text{Cl}^i_{12}\}\text{Cl}^a_6\}^{n-}$ series. The only experimental structure built from a cluster unit of composition closest to an aquo-cluster [$\{\text{Nb}_6\text{Cl}^i_{12}\}(\text{H}_2\text{O})^a_6\}^{2+}$ is that of [Nb₆Clⁱ₁₂(\text{OH})^a₂(\text{H}_2\text{O})^a₄].4\text{H}_2\text{O} built up from the aquo-hydroxo [Nb₆Clⁱ₁₂(\text{OH})^a₂(\text{H}_2\text{O})^a₄] ³³

containing four water molecules and two hydroxo groups in apical positions. In that structure, numerous hydrogen bond-type interactions involve water molecules from the cluster units and those from the network of water crystallization molecules. A full solid-state geometrical relaxation would be necessary to simulate this arrangement in which the H₂O apical ligands are partly deprotonated. Interestingly, the optimized geometry of the 16-VEC $[\{\text{Nb}_6\text{Cl}^i_{12}\}(\text{H}_2\text{O})^a_6]^{2+}$ cluster unit based compounds shows Nb-Nb and Nb-Clⁱ bond-lengths really close to those found in the structure of $[\text{Nb}_6\text{Cl}^i_{12}(\text{OH})^a_2(\text{H}_2\text{O})^a_4]\cdot 4\text{H}_2\text{O}$ solved by single-crystal X-ray diffraction tools. This validates the computational protocol. The calculated Nb-O^a(H₂) distances are, however, a little bit longer than those of the experimental structure. This can be explained by the fact that the hydrogen bond network was not considered in the calculations.

In order to model, the vibrational fingerprints of $[\{\text{Nb}_6\text{Cl}^i_{12}\}\text{Cl}^a_2(\text{H}_2\text{O})^a_4]\cdot 4\text{H}_2\text{O}$, we tentatively tried to optimize the *trans*- $[\{\text{Nb}_6\text{Cl}^i_{12}\}\text{Cl}^a_2(\text{H}_2\text{O})^a_4]$ cluster unit surrounded by four water molecules. Since no crystal structure data are reported for $[\{\text{Nb}_6\text{Cl}^i_{12}\}\text{Cl}^a_2(\text{H}_2\text{O})^a_4]\cdot 4\text{H}_2\text{O}$, in the optimization calculations, the starting positions of the surrounding water molecules were taken from the parent experimental crystal structure of $[\{\text{Ta}_6\text{Br}^i_{12}\}\text{Br}^a_2(\text{H}_2\text{O})^a_4]\cdot 3\text{H}_2\text{O}$.²⁴ Grimme dispersion corrections were added to take into account long-range interactions.³⁵ This methodology was successfully applied to the optimization of the *trans*- $[\{\text{Ta}_6\text{Br}^i_{12}\}\text{Br}^a_2(\text{H}_2\text{O})^a_4]$ cluster units surrounded by four water molecules in $[\{\text{Ta}_6\text{Br}^i_{12}\}\text{Br}^a_2(\text{H}_2\text{O})^a_4]\cdot 3\text{H}_2\text{O}$.²⁴ Unfortunately, the interaction with the water molecules leads to Clⁱ (partial) de-coordination along with strong deformation of the cluster unit for the niobium chloride homologous whatever the constraints used (fixed distances or angles). A full solid-state geometrical relaxation would be necessary.

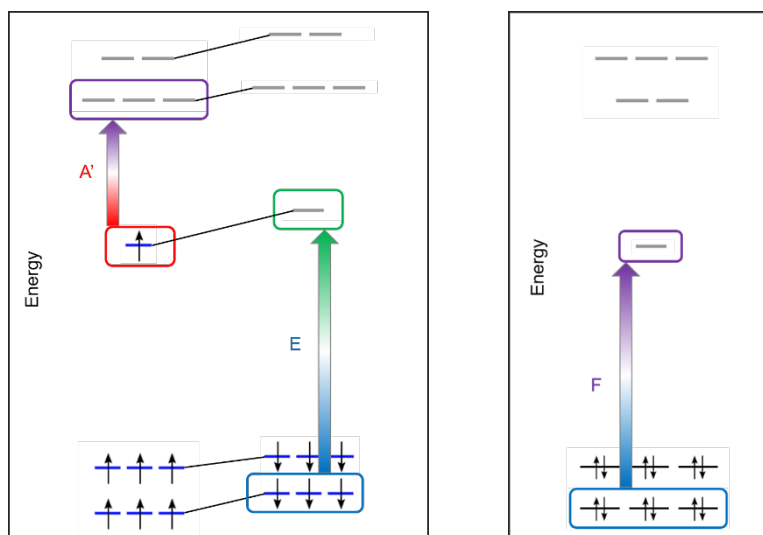
In order to get a better understanding of the electronic excitation properties of the series of studied compounds and of the experimental UV-visible absorption spectra of **1_{water}** and **1_{acetone}**, the electronic excitations of $[\{\text{Nb}_6\text{Cl}_{12}^i\}\text{Cl}_6^a]^{4-}$ (VEC = 16), $[\{\text{Nb}_6\text{Cl}_{12}^i\}(\text{H}_2\text{O})_6^a]^{2+}$ (VEC = 16), $[\{\text{Nb}_6\text{Cl}_{12}^i\}\text{Cl}_6^a]^{3-}$ (VEC = 15) and $[\{\text{Nb}_6\text{Cl}_{12}^i\}\text{Cl}_6^a]^{2-}$ (VEC = 14) were computed by TD-DFT calculations using the same level of theory as that used for the geometry optimization. The excitation energies and the nature of the main electronic excited states are described in Table S9 and depicted in Scheme 2. The simulated absorption spectra built using these data are given in Figure 5 (left). The main absorption peak of $[\{\text{Nb}_6\text{Cl}_{12}^i\}(\text{Cl})_6^a]^{4-}$ in the red-NIR region is mainly described by a HOMO to LUMO electronic transition (denoted **A** in Scheme 2). These MOs are delocalized over the Nb_6 octahedron. While the HOMO's character is metal-metal bonding, the three degenerated LUMOs (t_{1u} symmetry) are metal-metal antibonding as previously described.³⁴ The nature of this electronic excitation can be designated as a Nb_6 to Nb_6^* excitation. The first intense excitation in the red-NIR region calculated for the $[\{\text{Nb}_6\text{Cl}_{12}^i\}(\text{H}_2\text{O})_6^a]^{2+}$ cluster unit is of the same nature (Table S9). **B** and **C** electronic transitions are described in Table S9. They can be mainly described by electronic transitions from HOMO- n to LUMO+ m levels ($1 \leq n \leq 2$; $2 \leq m \leq 3$).



Scheme 2. Main electronic transitions represented by colored arrows between MOs of $[\{\text{Nb}_6\text{Cl}_{12}^{\text{i}}\}\text{Cl}_6^{\text{a}}]^{4-}$. The iso-surfaces of the MO representation: $\pm 0.02 \text{ e bohr}^{-3/2}$. Only one of the symmetrically equivalent degenerated MOs is depicted for the sake of clarity.

The consequence of two successive one-electron oxidations of $[\{\text{Nb}_6\text{Cl}_{12}^{\text{i}}\}\text{Cl}_6^{\text{a}}]^{4-}$ (leading to $[\{\text{Nb}_6\text{Cl}_{12}^{\text{i}}\}\text{Cl}_6^{\text{a}}]^{3-}$ and $[\{\text{Nb}_6\text{Cl}_{12}^{\text{i}}\}\text{Cl}_6^{\text{a}}]^{2-}$ respectively) on the absorption properties has been simulated. The appearance of low-energy electronic excitations in the red-NIR area was predicted from calculations for both oxidized cluster units. The simulated absorption spectrum of $[\{\text{Nb}_6\text{Cl}_{12}^{\text{i}}\}\text{Cl}_6^{\text{a}}]^{3-}$ presents two allowed low-energy excitations centered at 1242 nm (**E**) and 1055 nm (**A'**) whereas for $[\{\text{Nb}_6\text{Cl}_{12}^{\text{i}}\}\text{Cl}_6^{\text{a}}]^{2-}$ only large peak centered at 1152 nm (**F**) is calculated (Figure 5). The excitation centered at 1242 nm calculated for the 15-VEC compound is described by the following combination of transitions: 83% of HOSO α (highest occupied spinorbital) to LUSO $\alpha+1$ (lowest unoccupied spinorbital) and 10% of HOSO $\beta-3$ to LUSO β . The second-lowest energy band (**A'**) is a combination of the same transitions but with reverse contributions (14% and

84% respectively). The NIR **F** absorption band calculated for $[\{\text{Nb}_6\text{Cl}^{i}_{12}\}\text{Cl}^{\text{a}}_6]^{2-}$ (14-VEC) is an electronic excitation which is described as the formal transition from the HOMO-1 to the LUMO which nature is $(\text{Nb}_6\text{-Cl}^{\text{a}})^*$ to a Nb_6 . The main transitions are represented in Scheme 3.



Scheme 3. Electronic transitions represented by colored arrows between MOs of $[\{\text{Nb}_6\text{Cl}^{i}_{12}\}\text{Cl}^{\text{a}}_6]^{3-}$ (left) and $[\{\text{Nb}_6\text{Cl}^{i}_{12}\}\text{Cl}^{\text{a}}_6]^{2-}$ (right).

The experimental spectrum of **1_{acetone}** is compared to the computed spectra of $[\{\text{Nb}_6\text{Cl}^{i}_{12}\}\text{Cl}^{\text{a}}_6]^{3-}$ and $[\{\text{Nb}_6\text{Cl}^{i}_{12}\}\text{Cl}^{\text{a}}_6]^{2-}$ cluster units in Figure 5 (right). This comparison evidences that **1_{acetone}** (and **3_{acetone}**) are better described by the excitation properties of the $[\{\text{Nb}_6\text{Cl}^{i}_{12}\}\text{Cl}^{\text{a}}_6]^{3-}$ cluster units. Indeed, the computational results show a double peak in the NIR region only for $[\{\text{Nb}_6\text{Cl}^{i}_{12}\}\text{Cl}^{\text{a}}_6]^{3-}$ resulting from the specific open-shell electronic configuration of this 15-VEC species (Scheme 3).

The Raman active vibrational properties of several cluster compounds of the series were calculated. They are compared to the experimental data in Figure 6. The calculated Raman data depend on both the symmetry of the molecule and on its orientation (Cartesian coordinates) since the frequency-dependent polarizability is calculated in the x, y z directions. They are also sensitive to small variations of the bond lengths within the cluster units.

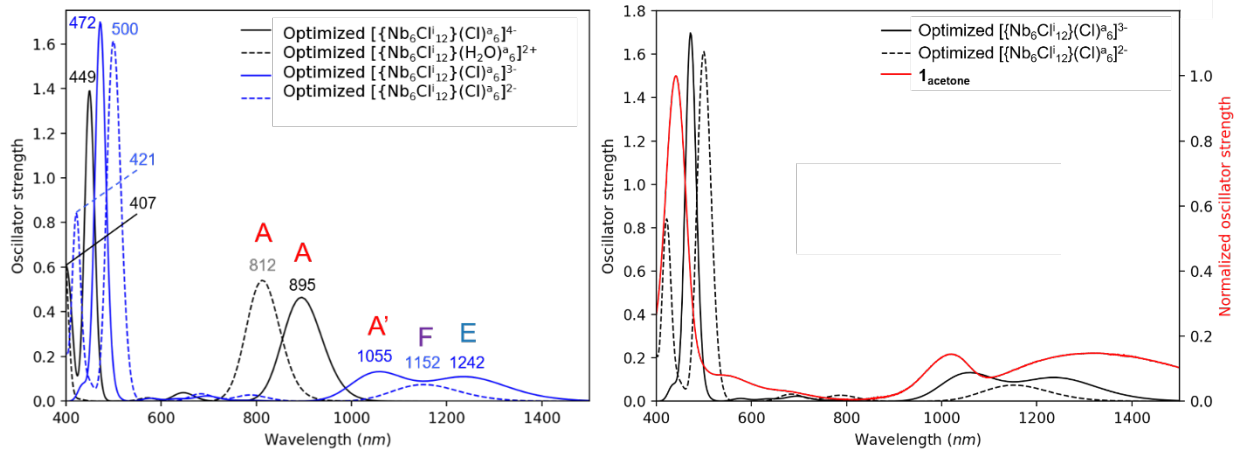


Figure 5. Left: Simulated absorption spectra of $[\{Nb_6Cl^{12}\}Cl^a_6]^{n-}$ ($n = 2-4$) and $[\{Nb_6Cl^{12}\}(H_2O)_6]^{2+}$. Right: Simulated absorption spectra of $[\{Nb_6Cl^{12}\}Cl^a_6]^{n-}$ ($n = 2-3$) compared to experimental absorption spectrum of **1**_{acetone}.

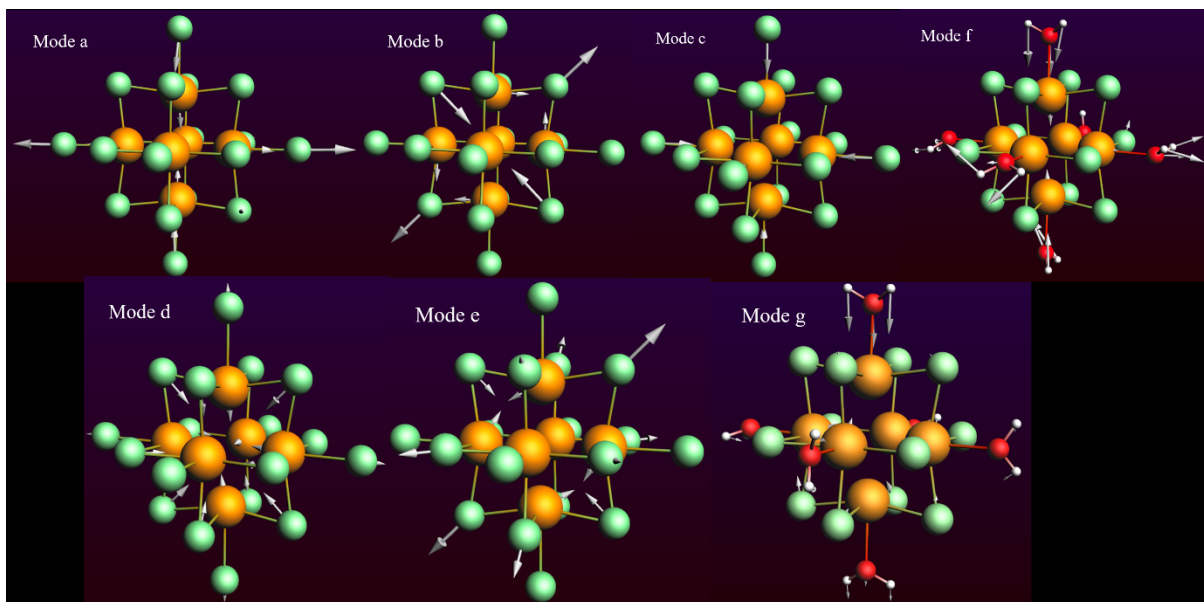


Figure 6. Normalized simulated Raman spectra of $[\{Nb_6Cl^{12}\}Cl^a_6]^{4-}$, $[\{Nb_6Cl^{12}\}(H_2O)_6]^{2+}$ and $[\{Nb_6Cl^{12}\}Cl^a_6]^{3-}$ cluster units (red curves) compared respectively to **1**, **1**_{water} and **2**, and **3** powder experimental Raman spectra (black curves).

They are also sensitive to small variations of the bond lengths within the cluster units. Given the knowledge gained from studying the parent tantalum bromide compound $K_4[\{Ta_6Br^{i}_{12}\}Br^a_6]$ and derivatives,²⁴ the comparison between simulated and experimental solid-state Raman data and further interpretations are significantly improved when the calculations use as input data, the atomic positions and the geometric parameters obtained from crystal structures. However, it is important to emphasize that the crystal structures obtained from the X-ray diffraction data provide cluster units with an average symmetry and average atomic positions. These averaged units often exhibit higher symmetries than true local symmetries. It may be therefore necessary for a better comparison between simulation and experimental results i) to consider the geometries adopted by the molecules in the experimental conditions and not the average ones extracted from crystal structures issued from X-ray diffraction, and/or ii) to consider the most stable optimized geometries obtained from simulations.

The simulated $[\{Nb_6Cl^{i}_{12}\}Cl^a_6]^{4-}$ Raman response was computed using the C_{2h} symmetry geometry issued from the crystal structure of $K_4[\{Nb_6Cl^{i}_{12}\}Cl^a_6]$ (space group: $C2/m$) obtained from single-crystal X-ray diffraction data reported by Simon *et al.*²³ It is compared to the solid-state Raman spectrum of **1** in Figure 6. Another comparison with the simulated Raman spectrum of $[\{Nb_6Cl^{i}_{12}\}Cl^a_6]^{4-}$ using the O_h symmetry is provided in Figure S10. On the other hand, for the 15-VEC species, the geometry of the $[\{Nb_6Cl^{i}_{12}\}Cl^a_6]^{3-}$ unit of C_I symmetry extracted from the crystal structure of **3** was used to perform the calculations. A comparison with the computed results obtained using the optimized O_h arrangement is given for sake of information in Figure S11. The simulated Raman response of $[\{Nb_6Cl^{i}_{12}\}Cl^a_6]^{3-}$ (C_I) compares really well with the experimental Raman spectra of **3** (Figure 6). Five main bands are observed above 100 cm^{-1} . The Raman active vibrational frequencies calculation at 135 cm^{-1} corresponds to coupled movement: a displacement

of all the atoms of the *pseudo*-axes C_2 towards the center of the octahedron, associated with the distance of all atoms from one of the *pseudo*-axes C_2 axes towards the center of the octahedron (mode *a*, Figure 7). The next band around 143 cm^{-1} corresponds to the superposition of three quasi-degenerated modes. Each mode can be described as follows: in a pseudo-plan of symmetry intersecting the octahedron, two *trans*- Cl^a are breathing in the while the two others are breathing out. The initial square shape of the four atoms of niobium in the plan is also impacted by the breathing, leading to a parallelogram (mode *b*, Figure 7). The most intense band at 195 cm^{-1} only involves the apical ligands which move in the direction of the center of the octahedron without the movement of the niobium atoms (mode *c*, Figure 7). The band at 265 cm^{-1} is a breathing of the whole cluster unit in which the Nb_6 and Cl_{12}^i are breathing in while Cl_6^a are breathing out (mode *d*, Figure 7). Finally, the more energetic band around 355 cm^{-1} corresponds to vibrational mode which is a tilt of Nb_4 basal plane associated with the cooperative asymmetric stretch of $\text{Cl}^i\text{-Nb-Cl}^i$ units (mode *e*, Figure 7). As explained in the experimental section, the Raman spectra of **1** and **3** built up from $[\{\text{Nb}_6\text{Cl}_{12}^i\}\text{Cl}_6^a]^{4-}$ and $[\{\text{Nb}_6\text{Cl}_{12}^i\}\text{Cl}_6^a]^{3-}$ cluster units respectively are highly similar with an overall offset of the order of cm^{-1} (Figure 3). This is not fully the case for the simulated Raman spectra of $[\{\text{Nb}_6\text{Cl}_{12}^i\}\text{Cl}_6^a]^{4-}$ in C_{2h} symmetry and of $[\{\text{Nb}_6\text{Cl}_{12}^i\}\text{Cl}_6^a]^{3-}$ in C_1 symmetry. The energy shifts in the band maxima are however of the same order of magnitude as the experimental ones (see for example the most intense peak around 250 cm^{-1}) but the intensities are not recovered for $[\{\text{Nb}_6\text{Cl}_{12}^i\}\text{Cl}_6^a]^{4-}$ (C_{2h}). It is indicative that the local symmetry of $[\{\text{Nb}_6\text{Cl}_{12}^i\}\text{Cl}_6^a]^{4-}$ in $\text{K}_4[\{\text{Nb}_6\text{Cl}_{12}^i\}\text{Cl}_6^a]$ is probably of lower symmetry than the C_{2h} symmetry imposed by the $C2/m$ space group of the crystal structure and which has been used in the simulation.²³ As stressed above, neither an experimental structure of **2** nor a structural modeling

of *trans*- $[\{\text{Nb}_6\text{Cl}^{i}_{12}\}-\text{Cl}^a_2(\text{H}_2\text{O})^a_4]$ surrounded by four water molecules have been obtained yet, precluding any simulation that could be compared to the Raman spectrum obtained for **2**.

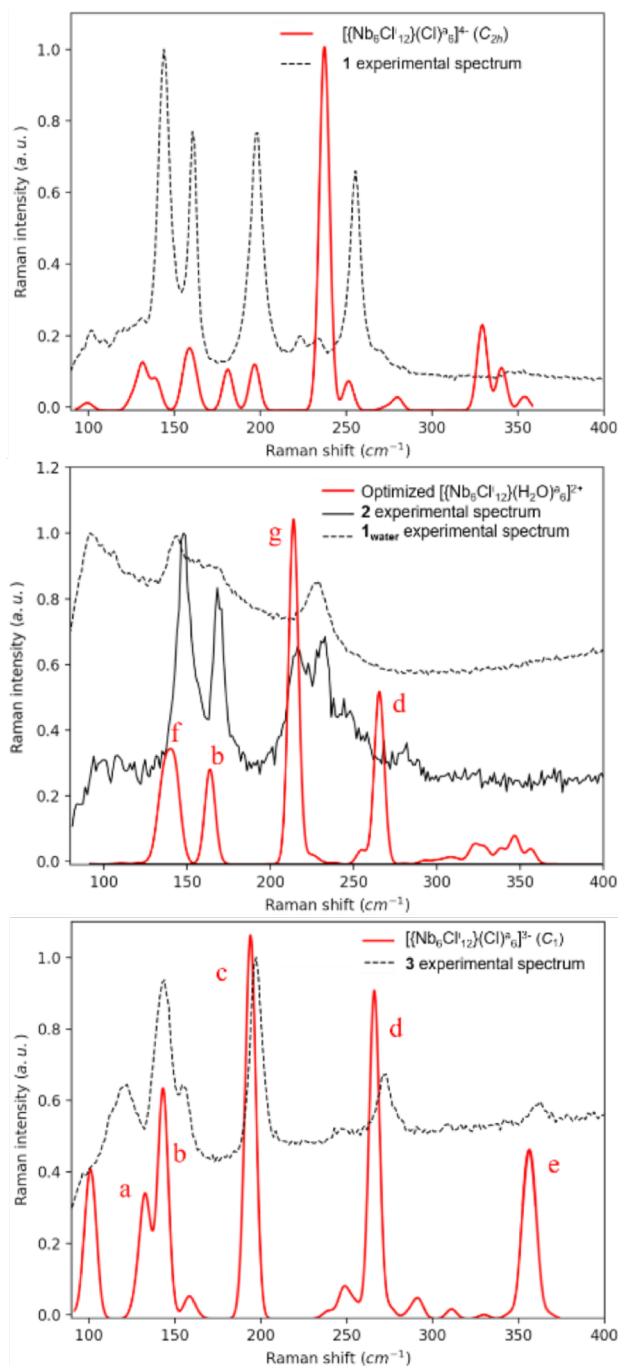


Figure 7. Representation of the Raman active vibrational modes of $[\{\text{Nb}_6\text{Cl}^{i}_{12}\}\text{Cl}_6]^{3-}$ and $[\{\text{Nb}_6\text{Cl}^{i}_{12}\}(\text{H}_2\text{O})_6]^{2+}$ annotated in Figure 6.

However, the Raman spectrum of the aqueous solution of $\mathbf{1}_{\text{water}}$ can be compared to the simulated Raman spectra of $[\{\text{Nb}_6\text{Cl}^{\text{i}}_{12}\}(\text{H}_2\text{O})^{\text{a}}_6]^{2+}$ which is, as demonstrated, earlier the most stable cluster unit in water. It is worth to mention that the aqueous solutions of $\mathbf{2}_{\text{water}}$ and $\mathbf{1}_{\text{water}}$ exhibit the same UV-vis-NIR absorption spectrum and the same mass spectroscopy results. These great similarities come from one and the same corresponding cluster fingerprint corresponding to that of the $[\{\text{Nb}_6\text{Cl}^{\text{i}}_{12}\}(\text{H}_2\text{O})^{\text{a}}_6]^{2+}$ units in solution. The Raman experimental spectrum of $\mathbf{1}_{\text{water}}$, the solid-state Raman spectrum of $\mathbf{2}$, and the simulated Raman spectra of the optimized $[\{\text{Nb}_6\text{Cl}^{\text{i}}_{12}\}(\text{H}_2\text{O})^{\text{a}}_6]^{2+}$ cluster cation are compared in Figure 6. As mentioned previously, the experimental Raman spectra of $\mathbf{1}_{\text{water}}$ and $\mathbf{2}$ mainly differ by the existence of an extra band at 216 cm^{-1} for $\mathbf{2}$. This extra vibrational frequency detected in $\mathbf{2}$ spectrum could be related to a vibration mode involving the Nb-Cl^a bonds but the impossibility to simulate the *trans*- $[\{\text{Nb}_6\text{Cl}^{\text{i}}_{12}\}\text{Cl}^{\text{a}}_2(\text{H}_2\text{O})^{\text{a}}_4]$ cluster unit surrounded by four water molecules precludes from any further interpretation. The computed $[\{\text{Nb}_6\text{Cl}^{\text{i}}_{12}\}(\text{H}_2\text{O})^{\text{a}}_6]^{2+}$ spectrum compares rather well the experimental spectrum of $\mathbf{1}_{\text{water}}$ except the mode *g* for which 2 peaks are observed experimentally (Figure 7). This mode can be characterized as a breathing of the whole octahedral cage associated to an important displacement of the axial H₂O^a-Nb-Nb-H₂O^a along the pseudo-*C*₄ axis (mode *g*, Figure 7). This mode involves importantly the water apical ligands and thus, the hydrogen bonding with the solvent is surely playing an important role that could be at the origin of the discrepancy between the simulated mode *g* and that experimentally observed. Explicit solvation effects should be implemented to simulate this aspect. Globally, the presence of water ligands makes more complex the vibrational modes compared to $[\{\text{Nb}_6\text{Cl}^{\text{i}}_{12}\}\text{Cl}^{\text{a}}_6]^{n-}$ vibrational frequencies since O(H)₂ motions are involved the active modes when apical ligands are implicated. The modes *b* and *d* which do not involve apical ligands are indeed retrieved in the simulated $[\{\text{Nb}_6\text{Cl}^{\text{i}}_{12}\}(\text{H}_2\text{O})^{\text{a}}_6]^{2+}$ spectrum (at 165 and

265 cm^{-1} respectively). The mode f for instance can be seen as deriving from mode a of $[\{\text{Nb}_6\text{Cl}_{12}^i\}\text{Cl}_6^a]^{n-}$ with combined $(\text{H}_2\text{O})^a$ motions.

4. FILMS PREPARATION AND CHARACTERIZATION

The protocols for embedding $\{\text{Nb}_6\text{Cl}_{12}^i\}^{m+}$ ($m = 2$ or 3) cluster core-based units in PVP from **1**, **2** and **3** are based on our previous works on Mo_6 and Ta_6 metal atom cluster compounds.^{7,36} They are sketched in Scheme 1 and are fully detailed in SI. In this study for **1** and **2**, only water was used as solvent instead of pure ethanol or ethanol-water mixture. Indeed, water was preferred to ethanol as solvent, although the drying step is slower, in order to prevent the oxidation of the cluster units that has been described before in this study for organic solvents. Several $\mathbf{1}_{\text{water}}$ solutions differing by the initial concentration of **1** were prepared. They were obtained by dissolution of **1** in distilled water (from 2.0 g.L^{-1} to 20.0 g.L^{-1}) and then filtered. Solutions and samples are denoted $\mathbf{1}_{\text{water-x}}$ where x denote the concentration. They range between the 2 extrema $\mathbf{1}_{\text{water-2.0}}$ and $\mathbf{1}_{\text{water-20.0}}$. Further dilutions or concentrations (by evaporation) of cluster solutions have been evaluated in order to obtain several values of FOM for sake of comparison. Different concentrations and molar mass of PVP were tested to get a compromise between viscosity, thickness and cluster concentration. The best results were obtained for PVP exhibiting a molar mass of 1 300 000 g.mol^{-1} . This PVP (Sigma Aldrich, $M = 1\,300\,000\ \text{g.mol}^{-1}$) was then added (10% weight ratio) to the solution that was maintained under magnetic stirring until homogenization. Then, 1 mL of the solution was drop-coated on glass substrates ($7.5 \times 2.5\ \text{cm}$). Samples were kept under air atmosphere during 6 hours for a complete drying at room temperature. The experimental protocol was optimized in order to get reproducible films with uniform coating

and controlled thickness. The digital microscope images of a cross-section in the middle of the dried films show that the thickness of all samples is $58 \pm 2 \mu\text{m}$ (left of Figure 8).

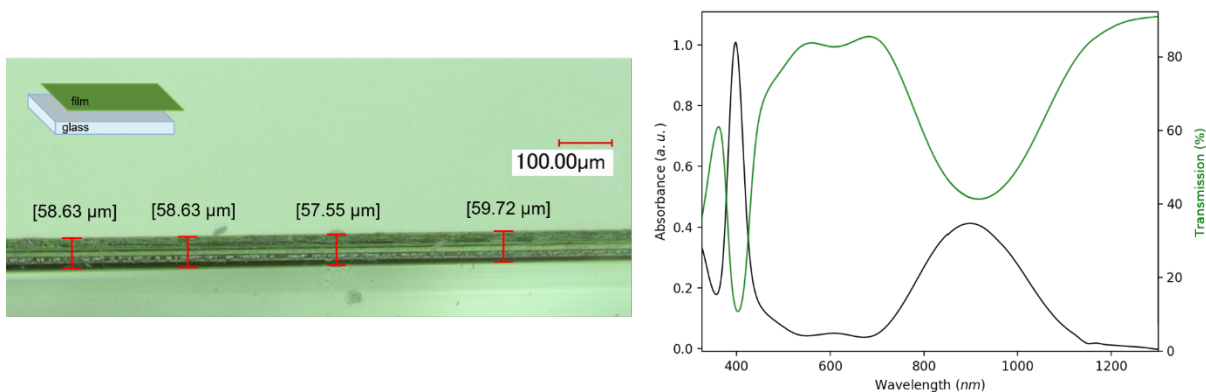


Figure 8. Left) Example of digital microscope pictures of the cross section of a $\{\text{Nb}_6\text{Cl}^{\text{i}}_{12}\}^{2+}@\text{PVP}$ films on glass substrate. Right) Normalized UV-visible absorption spectra of $\mathbf{1}_{\text{water}}$ (black) and UV-visible transmission spectra of the film.

The green olive color of the films suggests that no oxidation of the $[\{\text{Nb}_6\text{Cl}^{\text{i}}_{12}\}(\text{H}_2\text{O})^{\text{a}}_6]^{2+}$ occurred upon the addition of PVP in $\mathbf{1}_{\text{water}}$ neither upon coating and drying of $\{\text{Nb}_6\text{Cl}^{\text{i}}_{12}\}^{2+}@\text{PVP}$ films. Optical and vibrational properties of the $\{\text{Nb}_6\text{Cl}^{\text{i}}_{12}\}^{2+}@\text{PVP}$ films were characterized to evaluate the cluster core oxidation state. The transmission spectrum of a $\{\text{Nb}_6\text{Cl}^{\text{i}}_{12}\}^{2+}@\text{PVP}$ film was compared to the absorbance spectrum of $\mathbf{1}_{\text{water}}$ (containing $[\{\text{Nb}_6\text{Cl}^{\text{i}}_{12}\}(\text{H}_2\text{O})^{\text{a}}_6]^{2+}$ cluster units) and represented in the right part of Figure 8. Considering the experimental uncertainty, both spectra are hardly differentiable. Indeed, this comparison evidences that $\{\text{Nb}_6\text{Cl}^{\text{i}}_{12}\}^{2+}@\text{PVP}$ film contains 16-VEC cluster cores. No eye-perceived trace of oxidized $\{\text{Nb}_6\text{Cl}^{\text{i}}_{12}\}^{+3}$ cluster core was detected in coated films after one year of aging at room temperature in air. Moreover, Raman spectra of $\{\text{Nb}_6\text{Cl}^{\text{i}}_{12}\}^{2+}$ cluster units embedded in PVP film have been compared to a PVP film without clusters and to the spectra of $\mathbf{1}_{\text{water}}$ and $\mathbf{2}$ (Figure 9). Vibrational frequencies of the cluster unit and those corresponding to the PVP matrix are observed in the Raman spectra of the

$\{\text{Nb}_6\text{Cl}_{12}\}^{2+}@PVP$ sample. The vibrational frequencies between 200 and 250 cm^{-1} of $\{\text{Nb}_6\text{Cl}_{12}\}^{2+}@PVP$ sample are closer to **2** than to $\mathbf{1}_{\text{water}}$. This suggests that substitutions between two H_2O^a and two Cl^a occur during the drying step when embedded in PVP and thus that the cluster unit in $\{\text{Nb}_6\text{Cl}_{12}\}^{2+}@PVP$ composite is $\{\text{Nb}_6\text{Cl}_{12}\}(\text{H}_2\text{O})^a_4\text{Cl}_2^a]{}^0$ as in **2**.

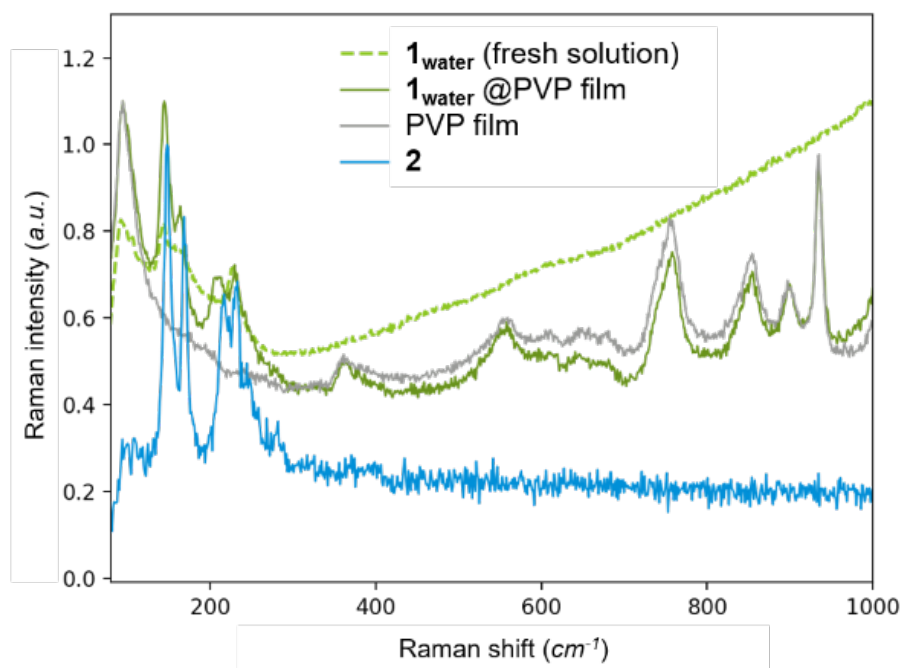


Figure 9. Normalized Raman spectra of $\mathbf{1}_{\text{water}}$ (solution), $\{\text{Nb}_6\text{Cl}_{12}\}^{2+}@PVP$ film (solid), a PVP control sample (solid), and **2** (solid).

Absorption spectra of chloride edge-bridged niobium clusters are characterized by a large band in the near-infrared region which are different depending on their oxidation state. This feature makes them attractive to be used as blocking filters building blocks for energy saving applications. For sake of optimization of NIR absorption of the $\{\text{Nb}_6\text{Cl}_{12}\}^{2+}@PVP$ films, the effects of the concentration of $\mathbf{1}_{\text{water}}$ on the optical properties and on the figure of merit (FOM) values were investigated. Solutions were prepared by dissolving up to 20.0 g of **1** per liter in water down to 2.0 g and filtered (notation: $\mathbf{1}_{\text{water}}\text{-}20.0 \rightarrow \mathbf{1}_{\text{water}}\text{-}2.0$; cluster unit concentration: $\sim 12.5 \text{ g}\cdot\text{L}^{-1}$ to $\sim 1.3 \text{ g}\cdot\text{L}^{-1}$).

¹). Above 20.0 g per liter, the dissolution is incomplete. Then, PVP is added to these solutions in a 10% weight ratio. After deposition and drying, the optical properties of the resulting $\{\text{Nb}_6\text{Cl}_{12}\}^{2+}$ @PVP films were measured from 250 to 2500 nm. Optical spectra of $\{\text{Nb}_6\text{Cl}_{12}\}^{2+}$ @PVP films are reported in Figure 10. The transmittance of the green olive films ranged from 61% at 915 nm for $\mathbf{1}_{\text{water}}-2.0$, the most dilute film to 1% at the same wavelength for $\mathbf{1}_{\text{water}}-20.0$, the stock solution.

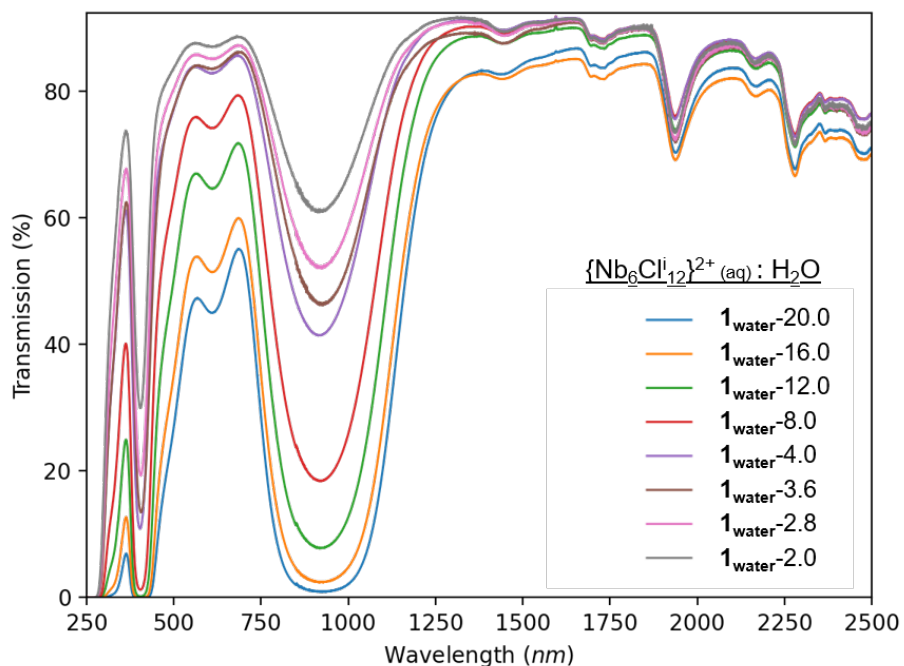


Figure 10. UV-visible transmission spectra of freshly prepared films of $\{\text{Nb}_6\text{Cl}_{12}\}^{2+}$ cluster unit embedded in PVP as a function of the concentration $\mathbf{1}_{\text{water}}$.

The color coordinates (x , y , z and $L^*a^*b^*$) and the FOM values (T_{vis} , T_{sol} , $T_{\text{vis}}/T_{\text{sol}}$ and S_{NIR}) were calculated for each film. These values are reported in Figure 11, Table 2 and S7. In order to check the reproducibility of the process and optical properties, sample preparations and measurements were repeated. The film thickness was 60 μm with a thickness variation of $\pm 5 \mu\text{m}$ from one batch to another. This variation induces an error bar on the CIE coordinates and

transmittance values of ± 0.01 and ± 1 respectively, showing a good reproducibility. The absorbance in the NIR-infrared region increases with the concentration of clusters in a film. The $T_{\text{vis}}/T_{\text{sol}}$ value thus rises until saturation, as point out in transmission mode in Figure 10. The highest reached value of $T_{\text{vis}}/T_{\text{sol}}$ is equal to 1.29 with a $T_{\text{vis}} > 50\%$. A T_{vis} value higher than 50% is indeed a mandatory condition for glass window applications.

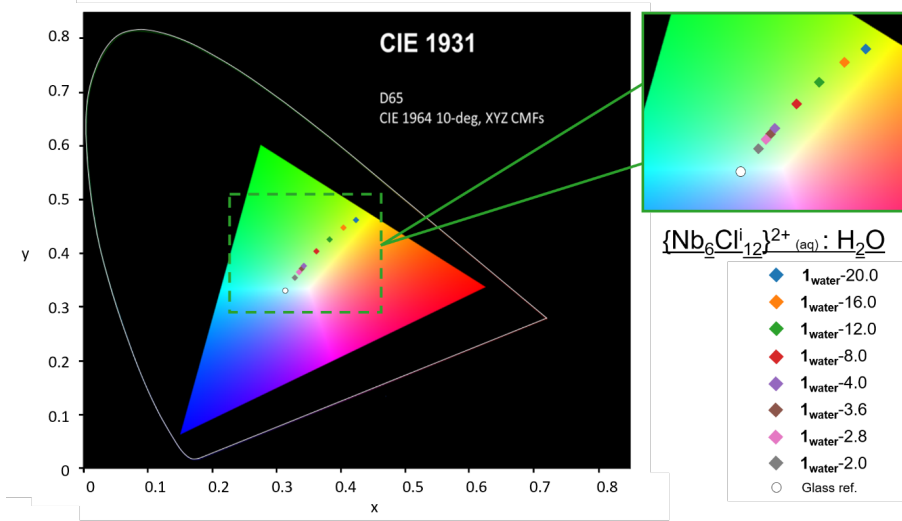


Figure 11. CIE chromaticity coordinates of films of different concentrations of $\{\text{Nb}_6\text{Cl}_{12}\}^{+2}$ cluster unit embedded in PVP. A glass substrate is used as a reference.

Table 2. CIE x, y and z color coordinates and the figure of merit (FOM) values of films of different concentrations of $\{\text{Nb}_6\text{Cl}_{12}\}^{+2}$ cluster unit embedded in PVP. Glass substrate is used for reference.

	x	y	z	T_{vis}	T_{sol}	$T_{\text{vis}}/T_{\text{sol}}$
$1_{\text{water}}-20.0$	0.423	0.463	0.113	41.5	33.8	1.2
$1_{\text{water}}-16.0$	0.404	0.448	0.147	48.5	38.0	1.3
$1_{\text{water}}-12.0$	0.382	0.427	0.190	62.2	48.3	1.3
$1_{\text{water}}-8.0$	0.362	0.404	0.233	72.3	57.9	1.2
$1_{\text{water}}-4.0$	0.339	0.372	0.289	81.9	70.5	1.2
$1_{\text{water}}-3.6$	0.343	0.378	0.279	82.0	71.5	1.1

$\mathbf{1}_{\text{water}}-2.8$	0.335	0.366	0.298	84.1	74.8	1.1
$\mathbf{1}_{\text{water}}-2.0$	0.329	0.356	0.315	86.4	78.8	1.1
Glass substrate	0.314	0.331	0.354	91.4	91.4	1.0

The reported color coordinates (Table 2) are presenting an increase of the x and y parameters related to the increase of the cluster concentration. The non-diluted film ($\mathbf{1}_{\text{water}}-20.0$) is described as yellowish green in the CIE representation (Figure 11) whereas the diluted ones tend to get closer to the glass substrate CIE values. As mentioned above, cluster species are known to be easily oxidized by oxygen under air atmosphere, the nature of the apical ligands and local pH being additional factors influencing the stability. The absorption spectra of the $\{\text{Nb}_6\text{Cl}_{12}\}^{2+}$ @PVP films which initially contain $\text{VEC} = 16 \{\text{Nb}_6\text{Cl}_{12}\}^{2+}$ cluster core have been measured after one month of aging at room temperature in air (Figure S5, S6, Table S2 and S7). It can be noticed that the films with $\{\text{Nb}_6\text{Cl}_{12}\}^{2+}$ concentration above $\mathbf{1}_{\text{water}}-12.0$ present an opacification phenomenon over days. It is particularly important for films prepared from the highest concentration, i. e., $\mathbf{1}_{\text{water}}-16.0$ and $\mathbf{1}_{\text{water}}-20.0$ (Figure S5). The overall transmission is highly affected by this opacification. The T_{vis} and T_{sol} parameters of the $\mathbf{1}_{\text{water}}-20.0$ and $\mathbf{1}_{\text{water}}-16.0$ films dropped from 41.5 and 32.3 to 17.3 and 13.1 respectively after few days of aging. At this stage, two hypotheses can be sketched out and they will be discussed below: i) the high concentration of cluster units may promote the aggregation of cluster units leading to diffusion phenomena, or ii) the high concentration of KCl impurities favors the transmission decrease. However, this phenomenon has no consequence on the $T_{\text{vis}}/T_{\text{sol}}$ nor on the CIE coordinates. Indeed, when comparing the samples ($\mathbf{1}_{\text{water}}-20.0$ to $\mathbf{1}_{\text{water}}-2.0$), the color coordinates (x, y and z) and the $T_{\text{vis}}/T_{\text{sol}}$ ratio are maintained regardless the aging of the $\mathbf{1}_{\text{water}}-20.0$ and $\mathbf{1}_{\text{water}}-16.0$ films. Since the CIE coordinates directly depend on the absorption spectra and thus to the VEC value of the cluster, it can be concluded that no oxidation upon aging is observed for the films. The reductant properties of PVP combined with the use of

$[\{\text{Nb}_6\text{Cl}^{\text{i}}_{12}\}(\text{H}_2\text{O})_6]^{\text{a}+2}$ intermediate in solution, prevent the formation of $\{\text{Nb}_6\text{Cl}^{\text{i}}_{12}\}^{\text{+3}}$ oxidized cluster core species in the final $\{\text{Nb}_6\text{Cl}^{\text{i}}_{12}\}^{\text{2+}}@\text{PVP}$ shaped composite films. In order to evaluate the influence of the VEC values on the optical properties of $\{\text{Nb}_6\text{Cl}^{\text{i}}_{12}\}^{\text{2+}}@\text{PVP}$ films, $\{\text{Nb}_6\text{Cl}^{\text{i}}_{12}\}^{\text{+3}}$ cluster core (VEC = 15) containing PVP films were prepared starting from **3_{DCM}** as cluster precursor solution as detailed in ESI. UV-Vis spectrum and FOM values are reported in Figure S7 and Table S3. As observed previously, the oxidation from VEC = 16 to VEC = 15 leads to a bathochromic shift. The 398 nm band is red shifted to 440 nm which induces a decrease of T_{vis} , whereas the large peak located at 899 nm is flattened and shifts approximately to 1000 and 1600 nm. Overall, the FOM values are highly impacted by the oxidation of the cluster core leading to $T_{\text{sol}} > T_{\text{vis}}$ and $T_{\text{vis}}/T_{\text{sol}} = 0.98$. Regarding those values, it can be concluded that oxidation of Nb_6 cluster units must be avoided for solar control applications. Niobium cluster units need to be maintained at their reduced state, *i.e.* VEC = 16 to ensure optimum near-infrared absorption property.

To clarify the role of KCl in the opacification process observed in highly concentrated **1_{water}** PVP films, two PVP films containing $\{\text{Nb}_6\text{Cl}^{\text{i}}_{12}\}^{\text{2+}}$ cluster units were prepared from solutions of **2** (*i.e.* without KCl byproduct) in water: one prepared from a highly concentrated solution and one presenting the best $T_{\text{vis}}/T_{\text{sol}}$ value for potential application for solar control. 12.5 and 6.0 g.L⁻¹ of **2** were necessary to reach similar concentration of $\{\text{Nb}_6\text{Cl}^{\text{i}}_{12}\}^{\text{2+}}$ cluster units as i) in **1_{water}-20.0**, ii) in **1_{water}-12.0**. The $\{\text{Nb}_6\text{Cl}^{\text{i}}_{12}\}^{\text{2+}}@\text{PVP}$ films, prepared from **2_{water}-12.5** and **2_{water}-6.0** respectively, were made by applying the same protocol than for **1_{water}** PVP films. Afterwards, in order to compare the aging of the selected films **1_{water}-20**, **1_{water}-12**, **2_{water}-12.5** and **2_{water}-6**, the CIE x, y and z color coordinates and the FOM were recorded after 24 h and after one month after their design (Table S4 and Table S5). Aging of the films was made by exposure under ambient

atmosphere near a normal window enabling day light and moon light exposures. It turns out that aging has no effect on the CIE coordinates. On the other hand, and as reported here above, for **1_{water}-20**, we note a strong decrease of both T_{vis} and T_{sol} but it has no effect on the ratio $T_{\text{vis}}/T_{\text{sol}}$ whatever the sample. For the films prepared from **2_{water}-12.5** and **2_{water}-6**, the characteristic values T_{vis} , T_{sol} , and $T_{\text{vis}}/T_{\text{sol}}$ are neither affected upon aging. To go deeper in the analysis, the haze values and the clarity of the films have been measured (Table S6) for the one-month aged samples. For the film prepared from **1_{water}-12**, the haze and clarity values become 12.2 % and 92.0 % respectively, values which are still acceptable for application purposes. On the other hand, **2_{water}-6** films exhibit unchanged very low haze and very high clarity: 1.4 % and 99.4 % respectively. This demonstrates that the KCl present in films prepared from **1** tends to crystallize upon time, favouring light scattering effects and consequently higher haze and lower clarity values than the films free of KCl or freshly prepared films.

The search for new materials in the field of glazing for energy saving applications is an emerging field of research. It appears that the light transmission coefficient (T_{vis}), energy transmission coefficient (T_{sol}) and the ratio $T_{\text{vis}}/T_{\text{sol}}$ are the most relevant characteristics to evaluate the performance of materials for solar control. To emphasize that niobium cluster containing composites exhibit very good NIR blocking properties, the NIR shielding values (S_{NIR}) were also calculated as described in ISI.³⁷ The S_{NIR} values are gathered in Table S7 for the prepared films 24 h and 1 month after their design. It is worth noting that as an emerging field of research, the number of research papers dealing with solar control composites where the T_{vis} , T_{sol} and $T_{\text{vis}}/T_{\text{sol}}$ or S_{NIR} values are reported is hitherto rather limited. Recently, Gao et al. reported the very high NIR shielding performance of CuS nanocrystals doped with Ga once embedded in an ethyl cellulose matrix and shaped as films. The S_{NIR} values of these films range from 46.1 to 72.4% depending on

the Ga/Cu molar ratio (0-0.06). It is worth noting that the films prepared from **1**_{water}-12.0 and **2**_{water}-6.0 exhibit high S_{NIR} values in the same range of S_{NIR} values as those reported by Gao *et al.*, *i.e.* 61.4 and 55.4% respectively. In terms of S_{NIR} values, the performance of {Nb₆Clⁱ₁₂}²⁺ cluster-core-based films is thus among the best of the composite films prepared to date. The other important feature is the T_{vis}/T_{sol} value. The reported values for the few developed glazing materials reported to date range from 1.0 for films prepared from gold nanorods,^{38,39} 1.01 for silver nanoprisms based films,⁴⁰ 1.24 for ITO,⁴¹ 1.11-1.23 for the series of cluster based films doped with {Ta₆Brⁱ₁₂}@PVP@ITO (1.25),⁸ {Nb₆Clⁱ₁₂}@PMMA@ITO (1.19),²⁰ ITO@{Nb₆Brⁱ₁₂}@SiO₂@ITO (1.11)⁴² up to 1.47 and 1.74 for films embedding tungsten oxides (for (NH₄)_xWO₃ and Cs_{0.32}WO₃ respectively).^{43,44} The T_{vis}/T_{sol} value for films prepared from **1**_{water}-12.0 and **2**_{water}-6.0 is 1.3. It compares rather well with the reported for composites embedding aluminum doped oxide (1.32).⁴¹

Compared to the cited inorganic compounds used for their NIR blocking properties in the design of solar control composites, the Nb₆ cluster compounds **1**, **2** and **3** are the only ones that are fully soluble in water (**1** and **2**) or in organic solvent (**3**). This solubility constitutes an important added value that favors an easy integration of Nb₆ cluster-based units in organic polymer and the easy shaping of the resulting composites. Thereby, the nanometer sized {Nb₆Clⁱ₁₂} cluster cores constitute in solution functional objects particularly suited for nanoarchitectonics.⁴⁵ According to K. Ariga, ‘*the concept of nanoarchitectonics is supposed to involve the architecting of functional materials using nanoscale units based on the principles of nanotechnology*’.⁴⁵ In that context, the added values of using {Nb₆Clⁱ₁₂} cluster core in the design of solar control composites compared to related systems reported in the literature, lies in the fact that there is no need to control i) the size of the crystallites as done for instance for tungsten bronze ceramics by ball milling, ii) the

aspect ratios as compulsory for nanoparticles or nanorods, iii) the dispersion in solutions necessary for the shaping of organic films.

5. CONCLUSIONS

We successfully prepared transparent $\{\text{Nb}_6\text{Cl}^{\text{i}}_{12}\}^{\text{m}+}\text{@PVP}$ nanocomposite films ($m = 2$ or 3) exhibiting both UV and NIR radiation blocking abilities for energy saving applications following an optimized procedure. Both experimental and theoretical approaches highlight that $[\text{Nb}_6\text{Cl}^{\text{i}}_{12}\text{Cl}^{\text{a}}_6]^{4-}$ cluster unit of the solid-state precursor $\text{K}_4[\{\text{Nb}_6\text{Cl}^{\text{i}}_{12}\}\text{Cl}^{\text{a}}_6]$ are sensitive to apical ligand substitutions and oxidation upon dissolution. Our study shows that optical properties are mainly related to the oxidation states (VEC) of the $[\{\text{Nb}_6\text{Cl}^{\text{i}}_{12}\}\text{Cl}^{\text{a}}_{6-x}(\text{H}_2\text{O})_x]^{m+/0/n-}$ ($x = 0, 4$ and 6) building blocks more than to the nature of the apical ligands. The understanding of the properties of the $[\{\text{Nb}_6\text{Cl}^{\text{i}}_{12}\}\text{Cl}^{\text{a}}_{6-x}(\text{H}_2\text{O})_x]^{m+/0/n-}$ cluster units thanks to several approaches (MS, Raman and UV-visible spectroscopies, electrochemistry and quantum chemical simulations) were crucial to optimize the shaping of the solar control composites. Concerning the integration of metal clusters as UV and NIR radiations blocking building blocks, we propose a straightforward method based on the use of either the crude solid-state ternary $\text{K}_4[\{\text{Nb}_6\text{Cl}^{\text{i}}_{12}\}\text{Cl}^{\text{a}}_6]$ precursor in compound **1** or the $[\{\text{Nb}_6\text{Cl}^{\text{i}}_{12}\}\text{Cl}^{\text{a}}_2(\text{H}_2\text{O})_4]\cdot 4\text{H}_2\text{O}$ compound **2**. Our methodology consists in stabilizing green olive reduced $\{\text{Nb}_6\text{Cl}^{\text{i}}_{12}\}^{2+}$ (VEC = 16) cluster core-based building block using a PVP polymer binder via a processing in aqueous solution. The $\{\text{Nb}_6\text{Cl}^{\text{i}}_{12}\}\text{@PVP}$ nanocomposite films that are obtained after drying are stable under atmosphere condition. They contain $[\{\text{Nb}_6\text{Cl}^{\text{i}}_{12}\}\text{Cl}^{\text{a}}_2(\text{H}_2\text{O})_2]^0$ as functional building blocks. The films prepared from a $12.0 \text{ g}\cdot\text{L}^{-1}$ solution of **1** or a $6.0 \text{ g}\cdot\text{L}^{-1}$ of **2** ($[\{\text{Nb}_6\text{Cl}^{\text{i}}_{12}\}\text{Cl}^{\text{a}}_2(\text{H}_2\text{O})_4]\cdot 4\text{H}_2\text{O}$) in a 10 % weight ratio of PVP ($M = 1\,300\,000 \text{ g}\cdot\text{mol}^{-1}$) present a FOM value ($T_{\text{vis}}/T_{\text{sol}}$) of 1.29. Such value is in the range of the values required for solar control applications. If **1** is used as precursor, only three integration steps are necessary for the fabrication

of the titled composite: the synthesis of **1**, its dissolution in water and stabilization in a polymer, and the shaping of glass coated films. For the highest concentrated films, the unreacted KCl present in **1** induce light scattering and consequently an increase in the haze value and a decrease of the clarity value. Interestingly, as shown in this study, the physical characteristics of moderately concentrated films are suitable for applications despite the presence of KCl. If needed, KCl-free films can be obtained by using **2** as source [$\{\text{Nb}_6\text{Cl}^{12}\}\text{Cl}^a_2(\text{H}_2\text{O})_2$]⁰ cluster units. This necessitates one additional preparation step.

In the context of nanoarchitectonics, Nb₆ cluster based functional building blocks constitute thus relevant nanoscale units for the design of solar control composites. The comparison of the optical performances of the titled materials with those of composites reported in the literature in terms of NIR shielding values (S_{NIR}) and T_{vis}/T_{sol}, places the $\{\text{Nb}_6\text{Cl}^{12}\}^{2+}$ @PVP nanocomposites among the best glass coating composites for energy saving applications. In the current literature dealing with the use of solid state compounds and nanoparticles for the design of solar control materials, the main challenge is to control the size and aspect ratios of crystallites or particles along the processing, and to control their dispersion in solution. The added values of using $\{\text{Nb}_6\text{Cl}^{12}\}$ cluster core composites is to overcome these limitations thanks to its well-defined composition and shape at the nanoscale that remains all along the integration steps, from the solid-state to its embedding in the organic PVP matrix.

ASSOCIATED CONTENT

Supporting Information. The Supporting Information is available free of charge at the <https://pubs.acs.org/doi/10.10XX/acsami.xxxxxxx>. Experimental procedures. Electrochemical measurements. X-ray powder patterns. UV-vis spectra. Photo-physical characterizations of

$\{\text{Nb}_6\text{Cl}_{12}\}^{2+}$ @PVP films (SEM image, UV-vis, FOM values, CIE coordinates, haze, clarity, NIR shielding values).

Accession Codes. CCDC 2125347 contains the supplementary crystallographic data **3**. These data can be obtained free of charge via www.ccdc.cam.ac.uk/data_request/cif, or by emailing data_request@ccdc.cam.ac.uk, or by contacting "The Cambridge Crystallographic Data Centre, 12 Union Road, Cambridge CB2 1EZ, UK; fax: +44 1223 336033".

Author Contributions

The manuscript was written through contributions of all authors. All authors have given approval to the final version of the manuscript. ‡These authors contributed equally.

AUTHOR INFORMATION

Corresponding Authors

Stéphane Cordier – Univ Rennes, CNRS, ISCR (Institut des Sciences Chimiques de Rennes) – UMR 6226, F-35000 Rennes, France; orcid.org/0000-0003-0707-3774

Karine Costuas – Univ Rennes, CNRS, ISCR (Institut des Sciences Chimiques de Rennes) – UMR 6226, F-35000 Rennes, France; orcid.org/0000-0003-0338-0494

Authors

Clément Lebastard – Univ Rennes, CNRS, ISCR (Institut des Sciences Chimiques de Rennes) – UMR 6226, F-35000 Rennes, France; CNRS – Saint-Gobain – NIMS, IRL 3629, Laboratory for Innovative Key Materials and Structures (LINK), National Institute for Materials Science, 1-1 Namiki, 305-0044 Tsukuba, Japan; orcid.org/0000-0002-4302-3603

Maxence Wilmet – CNRS – Saint-Gobain – NIMS, IRL 3629, Laboratory for Innovative Key Materials and Structures (LINK), National Institute for Materials Science, 1-1 Namiki, 305-0044 Tsukuba, Japan; Univ Rennes, CNRS, ISCR (Institut des Sciences Chimiques de Rennes) – UMR 6226, F-35000 Rennes, France; Saint-Gobain Research Paris, F-93300 Aubervilliers, France

Clothilde Comby-Zerbino – Univ Lyon, Université Claude Bernard Lyon 1, ENS de Lyon, Institut des Sciences Analytiques, UMR 5280, 5 rue de la Doua, F-69100 Villeurbanne, France.

Luke MacAleese – Univ Lyon, Université Claude Bernard Lyon 1, ENS de Lyon, Institut des Sciences Analytiques, UMR 5280, 5 rue de la Doua, F-69100 Villeurbanne, France;
orcid.org/0000-0001-8821-6049

Philippe Dugourd – Univ Lyon, Université Claude Bernard Lyon 1, ENS de Lyon, Institut des Sciences Analytiques, UMR 5280, 5 rue de la Doua, F-69100 Villeurbanne, France;
orcid.org/0000-0003-4395-1140

Tetsuo Uchikoshi – CNRS – Saint-Gobain – NIMS, IRL 3629, Laboratory for Innovative Key Materials and Structures (LINK), National Institute for Materials Science, 1-1 Namiki, 305-0044 Tsukuba, Japan; Research Center for Functional Materials, National Institute for Materials Science (NIMS), 1-1 Namiki, Tsukuba, Japan; orcid.org/0000-0003-3847-4781

Vincent Dorcet – Univ Rennes, CNRS, ISCR (Institut des Sciences Chimiques de Rennes) – UMR 6226, F-35000 Rennes, France; orcid.org/0000-0001-9423-995X

Maria Amela-Cortes – Univ Rennes, CNRS, ISCR (Institut des Sciences Chimiques de Rennes) – UMR 6226, F-35000 Rennes, France; orcid.org/0000-0002-5368-988X

Adèle Renaud – Univ Rennes, CNRS, ISCR (Institut des Sciences Chimiques de Rennes) – UMR 6226, F-35000 Rennes, France; orcid.org/0000-0002-7427-0148

Fabien Grasset – CNRS – Saint – Gobain–NIMS, IRL 3629, Laboratory for Innovative Key Materials and Structures (LINK), National Institute for Materials Science, 1-1 Namiki, 305-0044 Tsukuba, Japan; Univ Rennes, CNRS, ISCR (Institut des Sciences Chimiques de Rennes) – UMR 6226, F-35000 Rennes, France; orcid.org/0000-0002-4911-0214

ACKNOWLEDGMENTS

The French ANR is acknowledged for financial support (Project CLIMATE ANR-17-CE09-0018). The authors are very grateful to Bertrand Lefeuvre ISCR UMR 6226 CNRS - Université Rennes 1 (UR1) and Grégory Taupier from UMS 2001 CNRS - UR1, and Alain Moréac from IPR UMR 6252 CNRS-UR1. K. C. acknowledges support by the French GENCI agency for HPC resources which were performed at the CINES and IDRIS (grant A0080800649, A0100800649). C. L. and M.W. acknowledge the UR1, Saint-Gobain (SG), the Japanese National Institute for Materials Science (NIMS) and the French Centre National de la Recherche Scientifique (CNRS) for their financial support. A part of this work was carried out in the France-Japan international collaboration framework ICGP NIMS-UR1.

REFERENCES

(1) Granqvist, C. G. Electrochromics for Smart Windows: Oxide-Based Thin Films and Devices. *Thin Solid Films* **2014**, *564*, 1–38.

- (2) Mirrahimi, S.; Mohamed, M. F.; Haw, L. C.; Ibrahim, N. L. N.; Yusoff, W. F. M.; Aflaki, A. The Effect of Building Envelope on the Thermal Comfort and Energy Saving for High-Rise Buildings in Hot–humid Climate. *Renew. Sust. Energ. Rev.* **2016**, *53*, 1508–1519.
- (3) Zheng, L.; Xiong, T.; Shah, K. W. Transparent Nanomaterial-Based Solar Cool Coatings: Synthesis, Morphologies and Applications. *Sol. Energy* **2019**, *193*, 837–858.
- (4) Kanehara, M.; Koike, H.; Yoshinaga, T.; Teranishi, T. Indium Tin Oxide Nanoparticles with Compositionally Tunable Surface Plasmon Resonance Frequencies in the Near-IR Region. *J. Am. Chem. Soc.* **2009**, *131*, 17736–17737.
- (5) Abendroth, T.; Schumm, B.; Alajlan, S. A.; Almogbel, A. M.; Mäder, G.; Härtel, P.; Althues, H.; Kaskel, S. Optical and Thermal Properties of Transparent Infrared Blocking Antimony Doped Tin Oxide Thin Films. *Thin Solid Films* **2017**, *624*, 152–159.
- (6) Chao, L.; Bao, L.; Wei, W.; Tegus, O. A Review of Recent Advances in Synthesis, Characterization and NIR Shielding Property of Nanocrystalline Rare-Earth Hexaborides and Tungsten Bronzes. *Sol. Energy* **2019**, *190*, 10–27.
- (7) Renaud, A.; Wilmet, M.; Truong, T. G.; Seze, M.; Lemoine, P.; Dumait, N.; Chen, W.; Saito, N.; Ohsawa, T.; Uchikoshi, T.; Ohashi, N.; Cordier, S.; Grasset, F. Transparent Tantalum Cluster-Based UV and IR Blocking Electrochromic Devices. *J. Mater. Chem. C* **2017**, *5*, 8160–8168.
- (8) Nguyen, T. K. N.; Renaud, A.; Wilmet, M.; Dumait, N.; Paofai, S.; Dierre, B.; Chen, W.; Ohashi, N.; Cordier, S.; Grasset, F.; Uchikoshi, T. New Ultra-Violet and near-Infrared Blocking Filters for Energy Saving Applications: Fabrication of Tantalum Metal Atom Cluster-Based

Nanocomposite Thin Films by Electrophoretic Deposition. *J. Mater. Chem. C* **2017**, *5*, 10477–10484.

(9) Espenson, J. H.; McCarley, R. E. Oxidation of Tantalum Cluster Ions. *J. Am. Chem. Soc.* **1966**, *88*, 1063–1064.

(10) Cordier, S.; Perrin, C.; Sergent, M. Crystallochemistry of some new niobium bromides with (Nb₆Br₁₈) units: Structures of CsErNb₆Br₁₈ and Cs₂EuNb₆Br₁₈. *Z. Anorg. Allg. Chem.* **1993**, *619*, 621–627.

(11) König, J.; Dartsch, I.; Sperlich, E.; Guillamón, E.; Llusar, R.; Köckerling, M. Niobium Cluster Compounds with Protonated N-Base Cations. *Z. Anorg. Allg. Chem.* **2020**, *646*, 1531–1538.

(12) Sperlich, E.; Köckerling, M. Cation-Anion Pairs of Niobium Clusters of the Type [Nb₆Cl₁₂(RCN)₆][Nb₆Cl₁₈] (*R* = Et, ⁿPr, ⁱPr) with Nitrile Ligands RCN Forming Stabilizing Inter-Ionic Contacts. *Z. Naturforsch. B* **2020**, *75*, 173–181.

(13) Anokhina, E. V.; Essig, M. W.; Lachgar, A. Ti₂Nb₆Cl₁₄O₄: A Unique 2D-1D Network Combination in Niobium Cluster Chemistry. *Angew. Chem. Int. Ed.* **1998**, *37*, 522–525.

(14) Yan, B.; Zhou, H.; Lachgar, A. Octahedral Niobium Chloride Clusters as Building Blocks of Templated Prussian Blue Framework Analogues. *Inorg. Chem.* **2003**, *42*, 8818–8822.

(15) Flemming, A.; König, J.; Köckerling, M. New Hexanuclear Niobium Cluster Compounds with Pyridine and *N*-Methylpyrrolidone Ligands: [Nb₆Cl₁₂(pyr)₆][AlCl₄]₂ and [Nb₆Cl₁₂(NMP)₆][GaCl₄]₂: Hexanuclear Nb Cluster Compounds with Pyridine and *N*-methylpyrrolidone. *Z. Anorg. Allg. Chem.* **2013**, *639*, 2527–2531.

- (16) Pigorsch, A.; Köckerling, M. The Crystallization of Extended Niobium-Cluster Framework Compounds: A Novel Approach Using Ionic Liquids. *Cryst. Growth Des.* **2016**, *16*, 4240–4246.
- (17) König, J.; Dartsch, I.; Topp, A.; Guillamón, E.; Llusar, R.; Köckerling, M. Air-Stable, Well-Soluble $A^I_2[Nb_6Cl_{18}]$ Cluster Compounds (A^I = organic cation): A New Route for Preparation, Single-Crystal Structures, Properties, and ESI-Mass Spectra: Air-Stable, Well-Soluble $A^I_2[Nb_6Cl_{18}]$ Cluster. *Z. Anorg. Allg. Chem.* **2016**, *642*, 572–578.
- (18) König, J.; Köckerling, M. A Hexanuclear Niobium Cluster Compound Crystallizing as Macroscopic Tubes. *Chem. Eur. J.* **2019**, *25*, 13905–13910.
- (19) Kamiguchi, S.; Nagashima, S.; Chihara, T. Characterization of Catalytically Active Octahedral Metal Halide Cluster Complexes. *Metals* **2014**, *4*, 84–107.
- (20) Nguyen, N. T. K.; Dubernet, M.; Matsui, Y.; Wilmet, M.; Shirahata, N.; Rydzek, G.; Dumait, N.; Amela-Cortes, M.; Renaud, A.; Cordier, S.; Molard, Y.; Grasset, F.; Uchikoshi, T. Transparent Functional Nanocomposite Films Based on Octahedral Metal Clusters: Synthesis by Electrophoretic Deposition Process and Characterization. *R. Soc. open sci.* **2019**, *6*, 181647.
- (21) Fleming, P. B.; Mueller, L. A.; McCarley, R. E. Chemistry of Polynuclear Metal Halides. II. Preparation of Polynuclear Niobium Chloride and Bromide *Inorg. Chem.* **1967**, *6*, 1–4.
- (22) Parsons, J. A.; Vongvusharintra, A.; Koknat, F. W. High Temperature Conproportionation of Niobium Pentahalide and Niobium Metal; A Convenient Route to Hydrated Cluster Halides $Nb_6Cl_{14} \cdot 8H_2O$ and $Nb_6Br_{14} \cdot 8H_2O$. *Inorg. Nucl. Chem. Lett.* **1972**, *8*, 281–286.

(23) Simon, A.; Schnering, H. G.; Schäfer, H. Beiträge zur Chemie der Elemente Niob und Tantal. LXIX $K_4Nb_6Cl_{18}$ Darstellung, Eigenschaften und Struktur. *Z. Anorg. Allg. Chem.* **1968**, *361*, 235–248.

(24) Wilmet, M.; Lebastard, C.; Sciortino, F.; Comby-Zerbino, C.; MacAleese, L.; Chirot, F.; Dugourd, P.; Grasset, F.; Matsushita, Y.; Uchikoshi, T.; Ariga, K.; Lemoine, P.; Renaud, A.; Costuas, K.; Cordier, S. Revisiting Properties of Edge-Bridged Bromide Tantalum Clusters in the Solid-State, in Solution and *Vice Versa*: An Intertwined Experimental and Modelling Approach. *Dalton Trans.* **2021**, *50*, 8002–8016.

(25) Koknat, F. W.; Parsons, J. A.; Vongvusharintra, A. Metal Cluster Halide Complexes. I. Efficient Synthesis of Hydrated Hexanuclear Niobium and Tantalum Cluster Halides $M_6X_{14} \cdot 8H_2O$. *Inorg. Chem.*, **1974**, *13*, 1699–1702.

(26) MacKay, R. A.; Schneider, R. F. Experimental Evidence Concerning the Electronic Structure of the Nb_6Cl_{12} Cluster. *Inorg. Chem.* **1967**, *6*, 549–552.

(27) Koknat, F. W.; McCarley, R. E. Chemistry of Polynuclear Metal Halides. IX. Crystal and Molecular Structure of Bis(tetramethylammonium)hexachloro(dodeca- μ -chloro-hexaniobate), $[(CH_3)_4N]_2[(Nb_6Cl_{12})Cl_6]$. *Inorg. Chem.* **1972**, *11*, 812–816.

(28) Hughes, B. G.; Meyer, J. L.; Fleming, P. B.; McCarley, R. E. Chemistry of Polynuclear Metal Halides. III. Synthesis of Some Niobium and Tantalum $M_6X_{12}^{n+}$ Cluster Derivatives. *Inorg. Chem.* **1970**, *9*, 1343–1346.

(29) Koknat, F. W.; McCarley, R. E. Chemistry of Polynuclear Metal Halides. XI. Crystal and Molecular Structure of Tris(tetramethylammonium)hexachloro(dodeca- μ -chloro-hexaniobate), $[(\text{CH}_3)_4\text{N}]_3[\text{Nb}_6\text{Cl}_{12}]\text{Cl}_6$. *Inorg. Chem.* **1974**, *13*, 295–300.

(30) Prokopuk, N.; Weinert, C. S.; Kennedy, V. O.; Siska, D. P.; Jeon, H. J.; Stern, C. L.; Shriver, D. F. Synthesis and Structure of the Useful Starting Material $[\text{Bu}_4\text{N}]_3[\text{Nb}_6\text{Cl}_{12}(\text{OSO}_2\text{CF}_3)_6]$. *Inorg. Chim. Acta* **2000**, *300–302*, 951–957.

(31) Pénicaud, A.; Batail, P.; Coulon, C.; Canadell, E.; Perrin, C. Novel Redox Properties of the Paramagnetic Hexanuclear Niobium Cluster Halide $\text{Nb}_6\text{Cl}_{18}^{3-}$ and the Preparation, Structures, and Conducting and Magnetic Properties of Its One-Dimensional Mixed-Valence Tetramethyltetra(selena and thia)fulvalenium Salts: $[\text{TMTSF}$ and $\text{TMTTF}]_5[\text{Nb}_6\text{Cl}_{18}] \cdot (\text{CH}_2\text{Cl}_2)_{0.5}$. *Chem. Mater.* **1990**, *2*, 123–132.

(32) Fleming, P. B.; Mccarley, R. E. Chemistry of Polynuclear Metal Halides. IV. Electronic Spectra of Some Niobium and Tantalum $\text{M}_6\text{X}_{12}^{n+}$ Cluster Derivatives. *Inorg. Chem.* **1970**, *9*, 1347–1354.

(33) Brničević, N.; Planinić, P.; McCarley, R. E.; Antolić, S.; Luić, M.; Kojić-Prodić, B. Synthesis and Structural Characterization of Three New Compounds Containing $[\text{Nb}_6\text{Cl}_{12}]^{2+}$ Units as Hydrated Hydroxides. *J. Chem. Soc. Dalton Trans.* **1995**, 1441–1446.

(34) Kuc, A.; Heine, T.; Mineva, T. Niobium-Chloride Octahedral Clusters as Building Units for Larger Frameworks. *Struct. Chem.* **2012**, *23*, 1357–1367.

(35) Grimme, S.; Ehrlich, S.; Goerigk, L. Effect of the Damping Function in Dispersion Corrected Density Functional Theory. *J. Comput. Chem.* **2011**, *32*, 1456–1465.

- (36) Aubert, T.; Nerambourg, N.; Saito, N.; Haneda, H.; Ohashi, N.; Mortier, M.; Cordier, S.; Grasset, F. Tunable Visible Emission of Luminescent Hybrid Nanoparticles Incorporating Two Complementary Luminophores: ZnO Nanocrystals and $[\text{Mo}_6\text{Br}_{14}]^{2-}$ Nanosized Cluster Units. *Part. Part. Syst. Charact.* **2013**, *30*, 90–95.
- (37) Gao, Q.; Wu, X.; Huang, T. Greatly Improved NIR Shielding Performance of CuS Nanocrystals by Gallium Doping for Energy Efficient Window. *Ceram. Int.* **2021**, *47* (17), 23827–23833.
- (38) Xu, X.; Gibbons, T. H.; Cortie, M. B. *Gold Bull.* **2006**, *39*, 156–165.
- (39) Stokes, N. L.; Edgar, J. A.; McDonagh, A. M.; Cortie, M. B. *J. Nanoparticle Res.* **2010**, *12*, 2821–2830.
- (40) Carboni, M.; Carravetta, M.; Zhang, X. L.; Stulz, E. *J. Mater. Chem. C* **2016**, *4*, 1584–1588.
- (41) Garcia, G.; Buonsanti, R.; Llordes, A.; Runnerstrom, E. L.; Bergerud, A.; Milliron, D. J. *Adv. Opt. Mater.* **2013**, *1*, 215–220.
- (42) Chen, W.; Nguyen, T. K. N.; Wilmet, M.; Dumait, N.; Makrygeni, O.; Matsui, Y.; Takei, T.; Cordier, S.; Ohashi, N.; Uchikoshi, ; Grasset, F. *Nanoscale Adv.* **2019**, *1*, 3693–3698.
- (43) Kang, L.; Xu, W.; Wang, K.; Liang, W.; Liu, X.; Gao, F.; Lan, A.; Yang, Y.; Gao, Y. *Sol. Energy Mater. Sol. Cells* **2014**, *128*, 184–189.
- (44) Yao, Y.; Chen, Z.; Wei, W.; Zhang, P.; Zhu, Y.; Zhao, Q.; Lv, K.; Liu, X.; Gao, Y. *Sol. Energy Mater. Sol. Cells* **2020**, *215*, 110656.

(45) Ariga, K. Nanoarchitectonics: What's Coming next after Nanotechnology? *Nanoscale Horiz.* **2021**, 6 (5), 364–378.

SYNOPSIS

